INSTITUTO SUPERIOR TÉCNICO
Universidade Técnica de Lisboa

Image Reconstruction in Gamma-ray Telescopes:

A new method and its application to the GAW project

André Alves Pina

Dissertação para obtenção do Grau de Mestre em

Engenharia Física Tecnológica

Júri

Presidente: Prof. João Seixas

Orientador: Prof. Mário Pimenta

Vogais: Prof. Auxiliar Convidado Bernardo Tomé

Julho 2007

Acknowledgements

First and foremost I would like to thank Professor Mário Pimenta for the opportunity to work at Laboratório de Instrumentação e Física Experimental de Partículas (LIP), where this work was developed. I would also like to express my gratitude to the members of the Cosmics group: Bernardo Tomé, Sofia Andringa, Pedro Assis, etc.

A special thanks must go to Miguel Pato, Sara Valente and Ruben Conceição for the way they welcomed me and, specially, for the patience they had through out the year.

For everything they've done during the last five years, I must recognize the help all of my classmates provided me with. A big thank you to Inês Souta, Elizabeth Cruz, Francisco Pedro, Miguel Pato, Mariana Cardoso, Frederico Fiúza, Elsa Abreu and everyone else. You've really been there when I needed.

To all of my friends outside of IST for constantly reminding me that there's life besides Physics and IST!

And most importantly, I want to say thank you to my parents and my brother for all the support they gave me.

Resumo

O estudo de Raios Gama de Muito Alta Energia é um campo recente mas muito activo. Vários detectores terrestres foram construídos para detectar estas partículas muito energéticas. A técnica utilizada é a técnica de Imaging Atmospheric Cherenkov Technique, que consiste na colecção da luz de Cherenkov emitida pelas Cascatas Atmosféricas Extensas que ocorrem quando uma partícula atravessa a atmosfera. Estes detectores são caracterizados por um grande sistema óptico com pequenos Campos de Visão. A intensa luz de fundo dá origem ao problema de separação entre cascatas iniciadas por fotões e cascatas iniciadas por protões. Um inovador método de separação Gama/Protão é apresentado neste trabalho. As diferenças entre cascatas originadas por Gamas e por Protões são notórias em dois aspectos principais. O primeiro é a largura da cascata e o segundo é a distribuição dos ângulos de emissão dos fotões de Cherenkov em relação ao eixo principal da cascata. Com mais do que um telescópio IACT, e as suas respectivas imagens bi-dimensionais de direcções de chegada dos fotões de Cherenkov, as características 3D da cascata podem ser reconstruídas. Os métodos desenvolvidos foram aplicados ao caso de GAW, um futuro detector com um grande Campo de Visão. Um poster sobre este trabalho estará presente na 30^{th} International Cosmic Ray Conference (Mérida, México) em Julho de 2007. Uma apresentação oral terá lugar na 6^{th} New Worlds in Astroparticle Physics (Faro, Portugal) em Setembro de 2007.

Palavras-chave:

Raios Gama de Muito Alta Energia, Cascatas Atmosféricas Extensas, Emissão de Luz de Cherenkov, Gamma Air Watch, Separação Gama/Protão

Abstract

The research on Very High Energy Gamma Rays is a recent but very active field. Many ground detectors have been conceived to detect these very energetic particles. The method used is the Imaging Atmospheric Cherenkov Technique, that consists in the collection of the Cherenkov light emitted by the Extensive Air Shower that originates when a particle crosses the atmosphere. These instruments are characterized by large optical systems with small Fields of View. The intense background light raises the problem of separating gamma showers from proton ones. A new approach to Gamma/Proton separation algorithms is proposed. The differences between Gamma and Proton showers are notorious in two main aspects. The first is the wideness of the shower, and the second is the distribution of emission angles of Cherenkov photons in respect to the shower main axis. Using more than one IAC telescope, and their respective bi-dimensional images of arrival direction of the Cherenkov photons, the 3D geometrical characteristics of the shower can be reconstructed. The developed methods are applied to the GAW case, a future detector with large Field of View. A poster focusing this work will be present at the 30^{th} International Cosmic Ray Conference (Mérida, México) in July 2007. Also an oral presentation will be held at the 6^{th} New Worlds in Astroparticle Physics (Faro, Portugal) in September 2007.

Key-words:

Very High Energy Gamma Rays, Extensive Air Showers, Cherenkov Light Emission, Gamma Air Watch, Gamma/Proton Separation

Contents

List of Tables

List of Figures

Chapter 1

Introduction

The number of known sources of Very High Energy (VHE) γ-rays is very small when compared to the ones known in the High Energy range. Up to a few years ago, detection was made with satellite detectors. However, due to the small flux for energies in the order of TeV, these events were extremely rare and the detection of sources was highly unlikely.

By the end of the 80s a new detection method for very energetic γ-rays was implemented. The passage of a particle through Earth's atmosphere creates a shower of particles, where the charged ones emit Cherenkov photons whenever their velocity is higher than the velocity of light in the atmosphere. The new method consists in collecting the Cherenkov photons emitted in the shower development and producing a bi-dimensional image of the arrival directions of these photons. This method was called Imaging Atmospheric Cherenkov Technique. It was with this technique that the Whipple Observatory (Az., USA) detected, in 1989, the Crab Nebula, a steady source of TeV γ-rays that is frequently used for calibrations. Since then, many ground based experiments have been developed.

These detectors are characterized by having large optic systems with small Fields of View (FoV). This difficults the task of discovering new VHE γ-ray sources as a sky survey would take a very big amount of time. Also, the existence of an intense background light further complicates this task, and an efficient γ/proton separation algorithm is needed. In this work, a new separation algorithm using 3D variables is proposed. Also, a new geometrical event reconstruction method is presented.

The basics about γ-rays are explained in chapter 2, and a historical context is established. An association between the energy of the γ-ray and the appropriate detection technique is made. Usually γ-rays in the High Energy Range (30 MeV to 100 GeV) are detected with Satellites, while Very High Energy γ-rays (100 GeV to 100 TeV) are detected using Ground detection techniques. The main characteristics and principles behind these techniques are discussed and compared, with the major present and future experiments from both being introduced. A brief review of current results and future prospects is also given.

The most commonly used technique for Very High Energy γ-rays is the Imaging Atmospheric Cherenkov (IAC) Technique. To understand this technique, one must first know the processes by which an Extensive Air Shower (EAS) is originated by the passage of a particle through the atmosphere. This is explained in chapter 3, where EAS started by γ and Protons are characterized and compared. The production of Cherenkov light by the secondary particles belonging to the showers is also addressed here as it is one of the fundamental processes for this work. To test the proposed methods, γ and proton showers were simulated using CORSIKA. The options used are indicated, as well as the simulation parameters.

One of the main future IAC Technique projects is the Gamma Air Watch (GAW) detector. The main

goals of this project, and its specifications, are presented in chapter 4. This experiment will be characterized by a large FoV due to the use of a Fresnel Lens as light collector and by the use of the single photoelectron counting as working mode for the photomultipliers on the focal plane. The proposed configuration for the telescopes of GAW was used to test the new methods.

The new 3D variables used to reconstruct and separate γ and proton showers are the angle of emission of the Cherenkov photons (α) and the impact parameter (b). α is the angle between the arriving directions and the shower main axis, while b is the minimum distance between the arriving photons path and the shower main axis. The point in the photons path closest to the shower main axis can be understood as being an approximation to the emission point of the Cherenkov photon. These variables are explained in detail in chapter 5, with the main differences between γ and proton showers being discussed.

Using these variables, a 3D geometrical reconstruction method that was developed and is explained in chapter 6. This method consists of two different phases. In phase I, an initial guess is made about the shower main axis and the shower core position using the bi-dimensional images of the arrival directions from each telescope. In phase II, an iterative procedure minimizes the distance of the emission points to the shower main axis until the shower core position is fixed.

With the reconstructed geometry of the shower, the distributions of the emission angles and the impact parameters for the available telescopes can be used to separate γ and protons showers. A previously used method and this new one are discussed in chapter 7. Two algorithms were built. One is a χ^2 value that measures how different from a γ shower the event is. In the second one, the likelihoods of an event being a γ or a proton shower are determined.

The results obtained for both methods are summarized in chapter 8, and also some conclusions are made about the work.

Chapter 2

Gamma-ray Physics

The Universe is seen differently at different wavelenghts, as the objects that populate it do not emit electromagnetic radiation at all wavelenghts. Therefore, in order to know it, it is necessary to perform studies through all of the electromagnetic spectrum. This led to the creation of different techniques to observe the sky. Figure 2.1 shows the sky seen at different wavelengths.

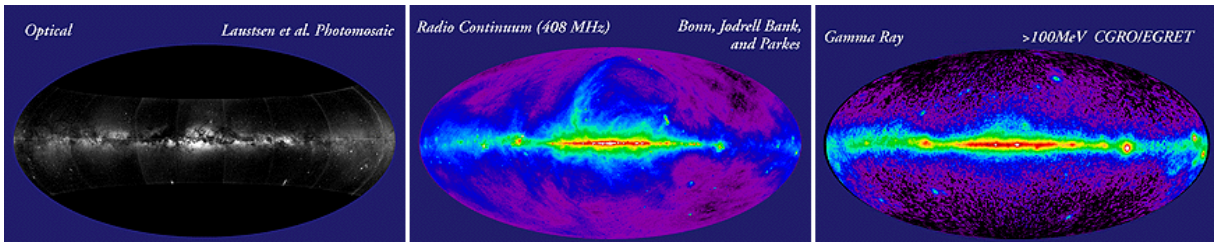

Figure 2.1: The sky seen at different wavelengths [1]

The first observations occurred in the visible band (350 nm to 750 nm), when Man came to exist. But it was only in the 19th century that people began looking at the Universe in the other bands. With the discoverement of different forms of light, invisible to the naked eye, new types of astronomy appeared. The first one to develop was the infrared astronomy (750 nm to 1 mm) around the middle of the 20th century, followed by radio astronomy (above 1 mm), X-ray (0.01 nm to 10 nm) and γ-ray (below 0.01 nm).

2.1 Gamma-rays

Gamma-rays are photons that arrive on earth from apparently random directions with energies that range from 1 MeV to a few thousands TeV. They can be classified by the energy with which they were emitted. Although there is not any definitive classification, most authors use the one shown in table 2.1 [2].

Even before any experiment was elaborated to detect Gamma-rays, scientists knew of their existence. Previous works had indicated that processes like the interaction of charged cosmic rays with the interstellar gas, supernova explosion and interactions between energetic electrons with magnetic fields occurred in the Universe, and with them, photon emission was mandatory.

They were first detected above the atmosphere in a balloon experiment, but the first important result was obtained in 1961 when Explorer-XI, the first γ-ray telescope, was put in orbit. This telescope

Energy Range	Gamma-ray Classification
1 to 30 MeV	Medium Energy
30 MeV to 100 GeV	High Energy
100 GeV to 100 TeV	Very High Energy
$\geq$ 100 TeV	Ultra High Energy

Table 2.1: Gamma-ray classification

detected over 100 cosmic photons that seemed to come from every direction in the Universe, implying some sort of uniform background radiation that would be expected from the interaction of charged cosmic rays with interstellar gas.

The detection of γ-rays depends on the energy they have, as this also has a direct connection with the main processes the photon suffers. For the Medium energy rays, the dominant interactions are Compton processes and as such, this type of Gamma-rays are detected using Compton telescopes. In the High and Very High Energy regions, pair production is used for detection.

Other very important aspect of Gamma-rays is their capacity to penetrate Earth's atmosphere. When they reach the atmosphere, a cascade of secondary particles is created. As some of these particles may travel at a velocity higher than the speed of light, they emit Cherenkov radiation that can be gathered at ground level to study the shower.

Medium and High Energy Gamma-rays are not able to penetrate the atmosphere deep enough to be detected, as the particles that are created in the atmosphere lose all of the energy through the already mentioned processes. This means that the detection of these types of photons has to occur above the Earth's atmosphere, typically in balloons or satellites.

For Very High Energy Gamma-rays, since satellite experiments are small and the flux of these very energetic photons is low, their detection is very hard with this approach. But, the cascades they produce in the atmosphere survive long enough to be studied. As such, ground detection methods have been developed that use the Imaging Atmospheric Cherenkov Technique [3]. This technique consists on imaging the flashes of Cherenkov radiation that are generated.

2.2 Satellite/Ground Detection

Satellite and Ground detectors for γ-rays have many differences between them, as the physics involved in each instrument has to be directed to the type of particle they can study. As it has been said, Satellite experiments are mainly used to study High Energy Gamma-rays, while Ground detectors are needed for the Very High Energy Gamma-rays.

2.2.1 Satellite detection technique

The first experiments in this area, used a "spark chamber" as the main component. This chamber was used to identify rays in the range of 30 MeV to 10 GeV, and it was used with great success in many satellites as SAS-2 (1973), COS-B (1975-1982) and CGRO (1991-2000). In figure 2.2, the "spark chamber" for the EGRET telescope in the CGRO satellite is shown.

Since the effective collection area is much smaller than the geometrical cross section of the telescope, its structure is very complex, comprising four main distinct components - the Tracker, the Trigger, The Calorimeter and the Veto.

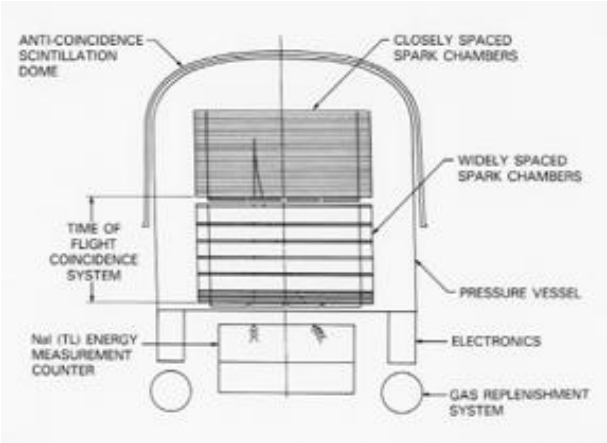

Figure 2.2: "Spark Chamber" schematics for CGRO experiment [4]

The Tracker

The Tracker consists of a series of parallel metal foils located in a close compartment, in which alternate foils are connected to each other electrically. When a charged particle passes through this chamber, a high voltage is applied to the second set of foils. The chamber contains a gas, noble gas-hydrocarbon mixture, at a pressure such that the passage of the charged particle originates an electrical discharge between the foils.

This means that an electron-positron pair created by the interaction of a γ-ray with one of the foils will be easily seen passing through the chamber as a pair of sparks will show the paths of both particles.

Actually, these paths are not linear as both particles suffer various scatterings inside the foils. This introduces a limitation on the size of the foils as they should be big enough to ensure the γ-ray interacts effectively, but not too thick so that the electrons do not suffer too many Coulomb Scatterings. The increase in the number of foils used allows for a better determination of the path of the electrons.

The collection area and the angular resolution of the telescope is determined by the geometry of the "spark chamber".

The Trigger

The trigger occurs when at least one electron manages to pass through the Tracker. The trigger then applies a high voltage on the second set of foils to activate the "spark chamber"

This high voltage cannot be maintained permanently as the electrical discharges could happen spontaneously. In order to avoid this, the application of high voltage is done with pulses.

The trigger system defined the Field of View (FoV) of the telescope, which is the region in space that the telescope can see.

The Calorimeter

To measure the energy of the electrons that pass through the telescope, they must be completely absorbed, and for this, a thick calorimeter is used.

Most of these telescopes use a NAI(Tl) crystal, whose only purpose is to measure the total energy that is deposited there.

In the lowest sensitivity region, the electrons energy can also be determined by the number of Coulomb scattering that occurs in the foils of the chamber.

The Veto

All of the previously mentioned components are surrounded by an anti-coincidence detector which gives the signal for an arriving charged particle but has a small cross section for the interaction with γ-rays.

Basically, this detector consists in a very thin outer "shell" of scintillation plastic with photomultipliers.

2.2.2 Ground detectors

Since the primary particle does not reach the ground level, one must gather all the information possible in order to extrapolate the direction and energy of the γ-ray. Since Cherenkov photons are emitted by every particle above the Cherenkov threshold, the atmosphere behaves as a giant calorimeter and thus, the measurement of light is a possible way to determine the energy of the primary γ-ray.

The Imaging Atmospheric Cherenkov Technique is used by many of the ground telescopes built so far. The first telescope to use this technique was the Whipple collaboration in 1984 [5].

This technique uses the atmosphere as collection area which allows for an effective collection area of several hundred square meters, and consists of creating an image of the brief flashes of Cherenkov radiation generated by the electromagnetic cascade [6].

A set of photomultipliers located at the focal plane of a big optical reflector is used to register the images, suffering a trigger whenever a predetermined number of photomultipliers detects a level of light above the threshold in a small time window. For each photomultiplier, this level is registered and the image is later analysed to determine if its characteristics are those of a γ-ray or other particle.

These detectors have a good angular resolution due to the fact that the emission angles of the secondary particles being small in respect to the primary particle direction. Roughly, the direction of the primary particle is the trajectory of the centre of the air shower.

As it has already been said, the quantity of light that is received by a detector at the earth's surface provides a good measure of the energy of the primary particle. The great uncertainty in this case is the distance to the centre of the shower. However, if this measurement occurs in the region between 50m to 130m of the shower core, the effect of the uncertainty is small. In these cases, with a set of parallel detectors it is possible to obtain an energy resolution of 10$\%$ to 15$\%$ [7].

The telescopes used in this technique (called Imaging Atmospheric Cherenkov Telescopes) comprise two main components: the Optic Reflector and the set of Photomultipliers.

Optical Reflector

To maximize the sensitivity of the detection of Cherenkov light, the collection area has to be as big as possible. An optical reflector is then used to maximize the collection, being composed of several small mirrors in an optical support with the focal distance being half of the curvature radius, thus obtaining the optimum optical image. The mirrors are normally made of glass, with the front part protected with aluminium and have a round or hexagonal shape.

Because of its big dimensions, the optical reflector is not protected with a cover, becoming susceptible to problems with the weather. To try and solve this, the aluminium surfaces are normally anodized and the mirrors are frequently cleaned.

Photomultipliers

The photomultipliers are small and fast detectors of light, having normally a maximum of quantum efficiency of about 15$\%$. Their disadvantages are mainly the fact that they operate in high voltage and that

they can be easily damaged with an excess of light.

One of the most expected developments in this area is the creation of photomultipliers with greater quantum efficiency that will allow the reduction of the energy threshold.

2.3 Present and Future Detectors

Since the beginnig of the 90s, the number of telescopes built to study γ-ray sources has grown at an amazing rate. The first major detector to study high energy γ-rays was the Compton Gamma-Ray Observatory (1991), while in the very high energy range, the Whipple Observatory (1989) was the first to obtain important results. Most notably, it detected the Crab Nebula which is a steady source of γ-rays in the TeV domain that is frequently used as a reference.

Currently, many detectors are studying and searching γ-ray sources. Due to the promising results obtained so far, and the obvious advancements in the instruments used, others are already planned for the near future. Some of the present and future detectors for high and very high energy emitters are discussed in the following sections.

2.3.1 Present detectors

Now-a-days, the main detector studying high energy γ-rays is the INTEGRAL satellite, which is an ESA mission with collaboration of the Russian Space Agency and NASA. The very high energy range is being studied by several collaborations, mainly HESS, VERITAS, CANGAROO and MAGIC. While MAGIC and HESS have been working for three or more years now, VERITAS is still very recent having started working this year.

INTEGRAL

INTEGRAL is acronym for International Gamma-Ray Astrophysics Laboratory [8] and is the most sensitive γ-ray observatory that was ever launched. Its main purpose is the study of violent and exotic objects in the Universe. Black holes, neutron stars, active galactic nuclei and supernovae, as well as Gamma Ray Bursts, are some of the objects in study. This is possible due to the good spectroscopy and the capability to image γ-ray emissions in the range of 15 KeV to 10 MeV.

Its main components are SPI, IBIS, JEM-X and OMC. SPI is the spectrometer to measure γ-ray energies with a high precision using an array of 19 hexagonal high purity germanium detectors that are cooled by a Stirling cooler system. This allows for a total detection area of 500 square centimetres.

IBIS is the imager used in INTEGRAL. It has a detector with a large number of pixels, all physically distinct from one another, which provides a fine imaging, source identification and spectral sensitivity to both continuum and broad lines. It is divided in two layers to allow the tracking of the photons in 3D, as they scatter and interact with many elements. This allows the improvement of the signal to noise ratio.

JEM-X is the joint European X-Ray Monitor, providing images in the 3 - 35 KeV prime energy band with an angular resolution of 3 arcmin. Here, the detector is an imaging micro strip gas counter that consists of two identical high pressure gas chambers, filled with a mixture of xenon and methane. This allows for the determination of the energy of the original X-ray.

The OMC is the optical camera. It allows long observations of the visible light coming from γ-ray and X-ray sources, being sensitive to stars with a visual magnitude up to 19.7.

HESS

HESS is an abbreviation for High Energy Stereoscopic System [9], in honor of Victor Hess who was the first to observe cosmic rays. Using four telescopes, the showers are observed under different viewing angles and the effective detection area is increased. The instrument was fully operational in December 2003 and is located in Namibia, being sensitive to γ-ray sources with intensities of a few thousand parts of the flux of the Crab Nebula.

The telescopes in HESS use the IAC technique. They are arranged in form of a square with 120 m side which allows for a simultaneous view of a single shower as they can be contained inside a Cherenkov light pool. The telescopes are supported by a "base frame" that can be rotated around a vertical axis and carries the dish (which rotates around the elevation axis), allowing it to be pointed to any point in the sky.

The mirror is composed of 382 round mirror facets made of aluminized glass with a quartz coating. It has a focal length of 15 m, with an arrangement that provides a good imaging also for off-axis rays. The total mirror area is 108 square metres for each telescope, with a reflectivity of more than 80$\%$.

The cameras of the telescopes capture and record the Cherenkov images of the air showers. The small pixel size, subtending an angle of 0.16°, provides a good resolution with a FoV of 5°. The camera is triggered by a coincidence of signals detected in 3 to 5 pixels in 8x8 pixel sectors. An effective coincidence window of about 1.5 ns is used, allowing for an efficient rejection of uncorrelated photomultipliers signals caused by photons of the night sky background. Also, only events that generate images in at least two telescopes are recorded.

MAGIC

MAGIC, which stands for Major Atmospheric Gamma-Ray Imaging Cherenkov Telescope [10], is located on La Palma in the Canaray Islands at an altitude of 2200 m above sea level. So far, it has achieved a threshold of 70 GeV, which is remarkable for a ground-based detector. A photograph of the telescope can be seen on figure 2.3.

Figure 2.3: MAGIC [10]

It is characterized by its large mirror, with an area of 236 square metres and a diameter of 17 m, that consists of nearly 1000 square elements of 49.5 cm x 49.5 cm. Due to the relatively lightness of the telescope, the reposition of the telescope axis can be done in less than a minute with the use of an automatic axis control. This is important as it allows the study of short-lived events as γ-ray bursts.

The camera used by MAGIC is a high-resolution one that is composed of 576 ultra-sensitive photomultipliers. The permanent digital sampling of the photomultiplier signal, at a rate of 300 MHz, permits a detailed time analysis.

VERITAS

The Very Energetic Radiation Imaging Telescope Array System (VERITAS) is a ground-based gamma-ray observatory with an array of four 12m optical reflectors [11], based on the Whipple Observatory. Each reflector is comprised of 350 individual facets with a total area of approximately 110 square metres.

The detectors have 499 pixels, of 2.86 cm diameter, corresponding each pixel to 0.15° which gives a total FoV of 3.5°. The use of reflecting light cones increases the overall photon collection efficiency.

To reduce the rate of triggers due to the night sky background, a two level trigger was implemented. Each channel is equipped with a constant fraction discriminator that produces a logic output pulse, of typically 10 ns, whenever the discriminator threshold is reached. The signal then passes a topological trigger system, which is used to detect pre-programmed patterns of triggered pixels in the camera.

CANGAROO

CANGAROO is an acronym for Collaboration of Australia and Nippon (Japan) for a GAmma Ray Observatory in the Outback [12]. It is a joint project of Australia and Japan, located near Woomera in South Australia.

The first telescopes was built in 1992, with a good quality mirror and a high resolution camera. A second telescope was built in 1999, called CANGAROO-II, with a 7 m diameter telescope. In 2000, the telescope was expanded to 10 m diameter so that the total light collection was increased. This expansion allowed the study of multi-hundred GeV energy region.

The expansion of the second telescope was just the begginig of the planned CANGAROO-III. It converted the previous telescope to be the first one of a set of four 10 m telescopes. The complete set was built by 2003, with the full operation beggining in 2004.

2.3.2 Future detectors

For the following years, many telescopes are already planned. In the high energy range, the GLAST satellite is the most expected detector with launch date scheduled for December 2007. As for the very high energy domain, MAGIC II, HESS II, CTA and GAW are in development. While MAGIC II and HESS II are extensions to the existing telescopes, CTA and GAW are new projects. CTA is still in study, while GAW is almost ready for construction. GAW will be discussed in a following chapter.

GLAST

GLAST, the Gamma-Ray Large Area SpaceTelescope, is a future satellite that will study astrophysical and cosmological phenomena in the high-energy domain [13]. It is expected that it will be sensitive from 5 KeV to 300 GeV. A schematics of GLAST can be seen in figure 2.4.

GLAST will have two main components, LAT and GBM. The Large Area Telescope (LAT) is an imaging γ-ray detector. As a photon hits one of the thin metal sheets of LAT it will convert to an electron-positron pair. These charged particles will pass through interleaved layers of silicon microstrips, causing ionization which can be detected as small pulses of electrical charge and allowing for the path of the

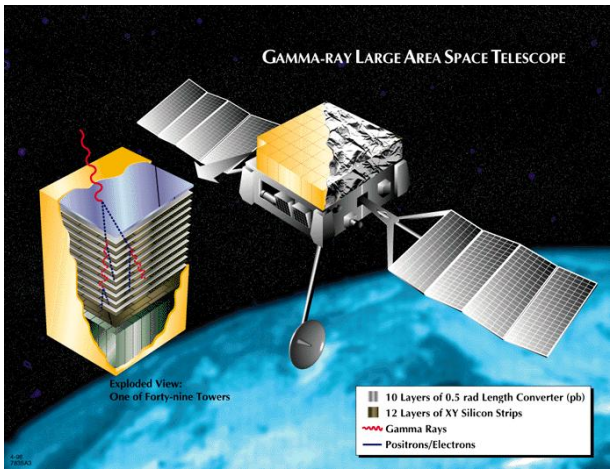

Figure 2.4: GLAST [13]

particles to be determined. The energy of the particles is measured by cesium iodide scintillator crystals that act as a calorimeter. LAT will have a large FoV of about 20% of the sky.

The GLAST Burst Monitor (GBM) will be used to detect γ-ray bursts and solar flares, mainly. It will include two sets of detectors: twelve NaI scintillators with a thickness of 1.27 cm and two cylindrical BGO scintillators of 12.7 cm height, all of them 12.7 cm in diameter. The scintillators will be positioned on the sides of the spacecraft to view all of the sky not blocked by earth.

HESS II

HESS II is an expansion of the current HESS observatory, in which a central very large telescope will be erected. This improvement will lower the energy threshold to 20 GeV and improve the sensitivity above 100 GeV [14].

This telescope will have a total mirror area of about 600 square metres, being made up of 850 mirror facets. Each pixel has a size of 0.07° for a FoV of 3.5°. The dish will be shaped as a curved rectangle, 32 m high and 24 m wide, with a depth varying from 2.7 m to 4.6 m.

The camera in HESS II follows what was done for the first stage, being composed of 2048 pixels [15]. It will be able to move along the optical axis in order to refocus the telescope depending on zenith angle to improve the image reconstruction. Also the readout front-end and the trigger have been redesigned to cope with the need of high velocity recording and transfer of signals and also to improve the rejection of triggers from the nigh sky background light.

MAGIC II

As with HESS, the MAGIC collaboration has decided to expand the current observatory by adding a new telescope [10]. The camera will be round with 1039 PMTs, of 0.1° and 35% quantum efficiency. Tests are still being performed to improve the quantum efficiency to 50% using silicon PMTs. The mirrors of the reflector will be square with side of 1 m.

While closely resembling MAGIC-I, MAGIC-II will be improved by using advanced photosensor with higher sensitivity, increased camera area with small-size pixels, mirror elements with large surface maintaining the total mirror area, improved non-interfering mirror adjustment and digital signal readout with improved time resolution.

CTA

The Cherenkov Telescope Array (CTA) is an observatory still in planning [16]. The propose is to build a large number of telescopes in a circle with the size of the telescopes decreasing from the centre to the outer parts. The telescopes will be built following the technologies used in HESS and MAGIC. The goal of this configuration is to create 2 or 3 zones in which the centre one will be a low-energy section with a threshold of about 15 GeV, the middle zone will be a medium-energy section with approximately 75 GeV threshold and a high-energy section with a threshold of 1 or 2 TeV.

CTA will have various modes of operation. In a deep wide-band mode all telescopes will be used to track the same source. The survey mode will be use to perform a sky survey. In search & monitoring mode, subclusters of the telescopes will track different sources. Other modes of operating are also planned.

Two different arrays are planned, a small one for the northern hemisphere to be located in the Canary Islands and a larger one for the southern hemisphere in Namibia.

2.4 Current Results

The first major VHE observations occurred in the 90s, when emissions from the Crab nebula were confirmed and new sources were discovered. These new sources were, however, only two pulsars (PSR 1706-44 and Vela) and two Active Galactic Nuclei with flares (Mkr 421 and Mkr 501). This clearly contrasted with the third EGRET Catalog that showed a rich sky of HE sources, as shown in fig. 2.5.

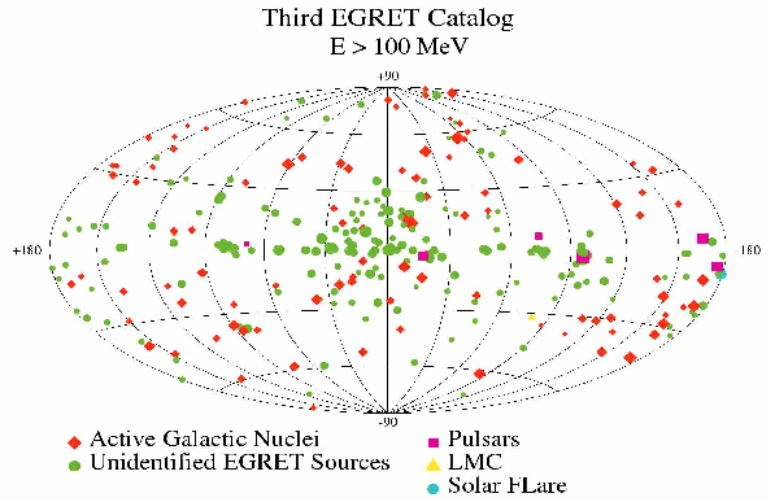

Figure 2.5: Third EGRET Catalog [1]

The development of the IACT technique brought a new approach on the VHE range and allowed for a more thorough search of sources. The number of known sources has been increasing at an impressive rate, and many more are expected to be found. Figure 2.6 shows the evolution of the number of VHE sources.

Following the construction of HESS and MAGIC, the most important ones, many discoveries were made. In what concerns Galactic observations, several Galactic sources were discovered by HESS, and also three by MILAGRO [17] and one by MAGIC, to which precision measurements of the spectra were made. Furthermore, theoretical models were developed based on these observations. New classes of

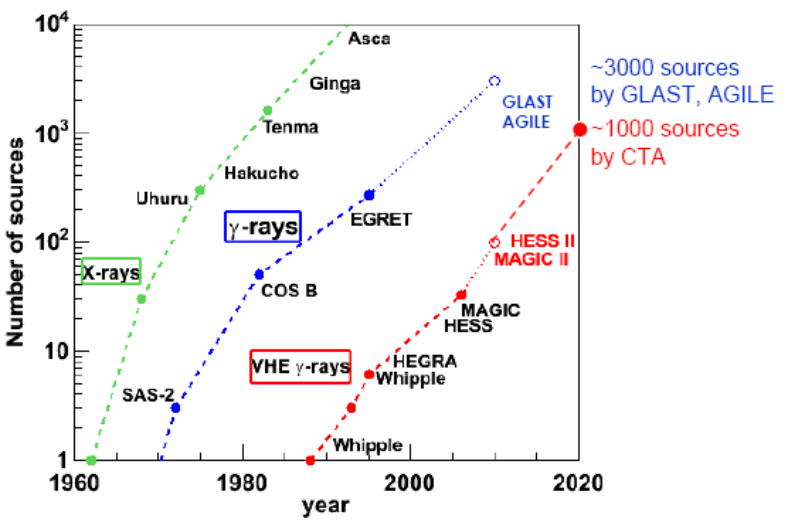

Figure 2.6: Number of known sources through time [1]

VHE γ-ray emitters were discovered by HESS and MAGIC such as a variable and a periodic galactic sources. The Galactic Centre was also studied, with the finding of evidence of a TeV signal.

Extragalactic observations were also performed with 15 new AGN being discovered, allowing the measurement of its properties and multi-λ studies. From the absorption spectrum, constraints on cosmological EBL density were made. MAGIC also observed an AGN with orphan flare, performed a high time-resolution study of AGN flares and did a Gamma-Ray Burst follow-up in coincidence with observation in the X-ray domain.

In March 2007, the number of known sources that emitted in the VHE range totals 47. Figure 2.7 shows the sky view of known sources.

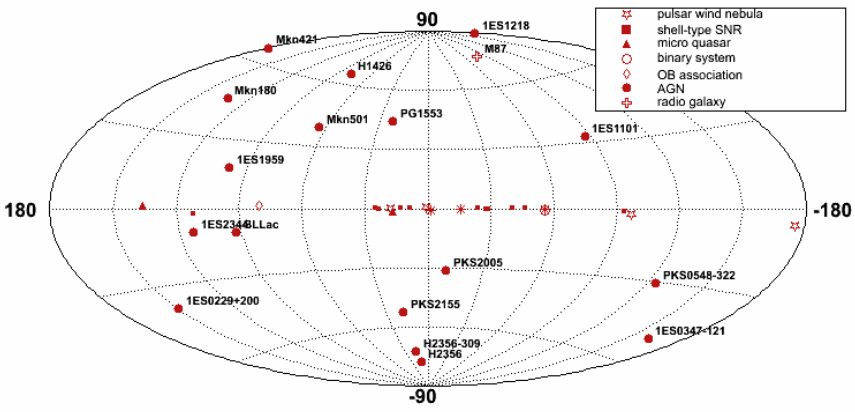

Figure 2.7: Sky view in the VHE range as of March 2007 [1]

Chapter 3

Extensive Air Showers

The earth is constantly being bombarded by cosmic particles and the study of these particles has shown that their flux obeys a power-law. The energy spectrum for cosmic rays can be seen in figure 3.1.

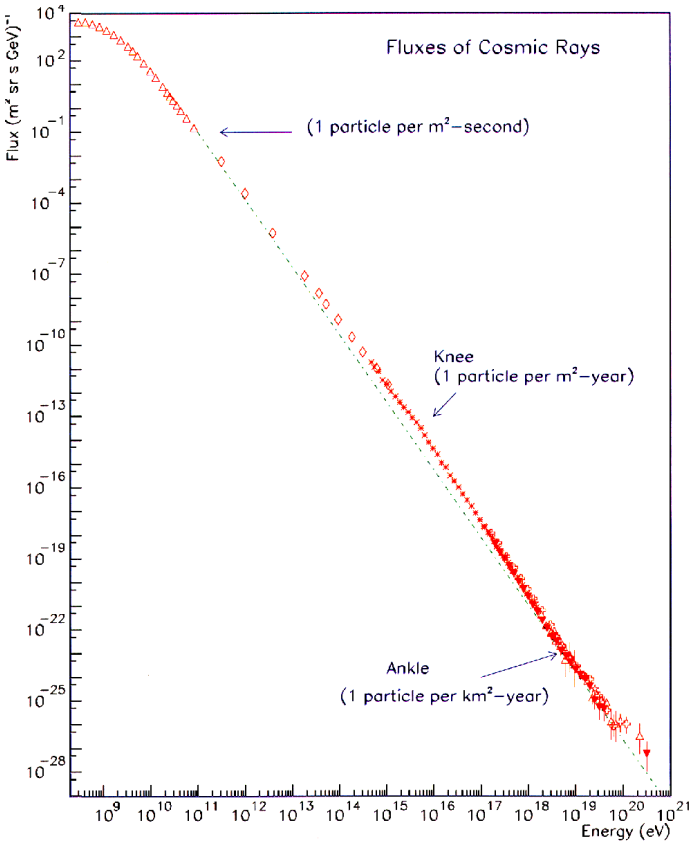

Figure 3.1: Energy spectrum for cosmic rays [18]

An extensive air shower is a wide cascade of ionized particles and electromagnetic radiation that is created when a cosmic particle enters the atmosphere. As the cosmic particle enters the atmosphere, an increasing number of particles belonging to the atmosphere may cross its path. Typically, the first interaction occurs at an altitude of about 20 Km, varying with the energy of the primary particle.

3.1 Characterization

The EAS are characterized by being a continuous process while the average energy is such that the losses in the ionization energies are equal to the losses by radiation. At this point the maximum number of electrons is reached and from there on, the number of particles diminishes and the cascade starts to die. The altitude where the this happens is known as shower maximum. Evidently, this point is dependant on the energy of the primary particle, getting closer to the ground as the energy increases.

As γ-rays enter the earth's atmosphere, they interact with the existing nucleus producing an electron-positron pair that shares the same energy as the primary γ-ray, travelling approximately in the same direction. These particles will interact with others through bremmstrahlung processes producing secondary γ-rays, who will in turn suffer pair production and so on, starting a chain of processes.

The angle of emission in these processes is proportional to $m_e c/E$ rad, where E is the energy of the electron. Therefore, the electromagnetic cascade is very compact around the primary Gamma-ray direction.

Other primary particles, such as protons, interact with atmospheric molecules typically producing charged mesons (e.g. pions and kaons). However, the fluctuations in the directions are bigger than in the electromagnetic cascades and as such, the shower is wider. A comparison between a Gamma-ray shower and a Nucleon shower can be seen in figure 3.2.

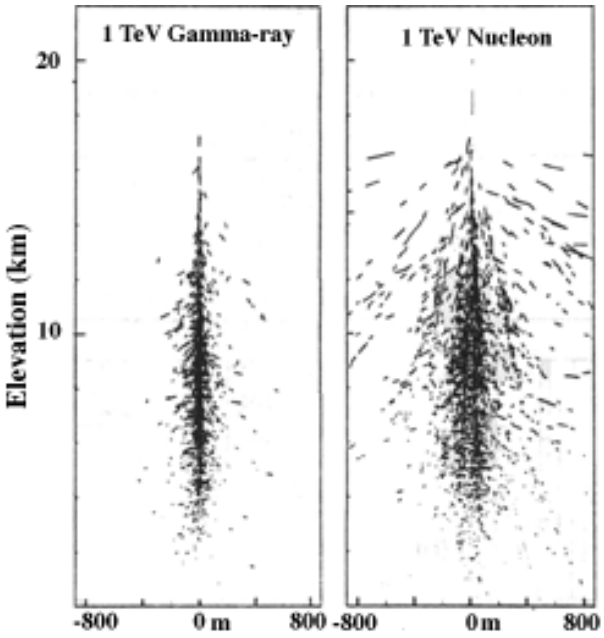

Figure 3.2: Comparison of Nucleon and Gamma-ray showers [19]

3.2 Cherenkov

One of the most important processes, and the fundamental one for this work, is the emission of Cherenkov radiation. As a charged particle travels through the atmosphere at a velocity higher than the speed of light, it disrupts the local electromagnetic field (EM). Electrons in the atoms of the atmosphere are displaced and polarized by the passing EM field of the charged particle. Photons are then emitted as the electrons restore themselves to equilibrium after the disruption has passed. While in normal cir-

cumstances, these photons destructively interfere with each other and no radiation is detected, if the disruption travels faster than the photons themselves, the photons constructively interfere and intensify the observed radiation.

The emitted photons move as a shock wave. This can be understood by the construction of a triangle. Considering that the charged particle (in red) moves with speed v_p we can define $\beta = v_p/c$ where c is the speed of light. The Cherenkov photons (in blue) are light, and as such travel at a velocity $v_{em} = c/n$ with n being the refractive index.

In the given time t, the particle travels x_p (cf. eq. 3.1) while the electromagnetic waves travel x_{em} (cf. eq. 3.2). From here, it is possible to build the triangle shown in figure 3.3 and obtain θ (from eq. 3.3).

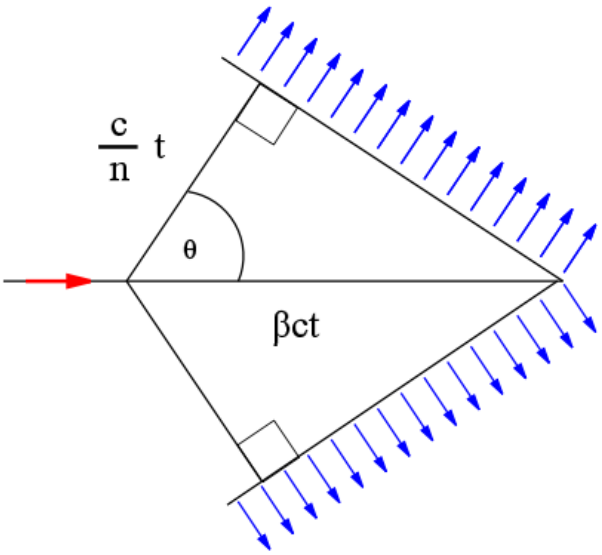

Figure 3.3: Geometry of Cherenkov radiation

$$x_p = v_p t = \beta c t \tag{3.1}$$

$$x_{em} = v_{em} t = \frac{c}{n} t \tag{3.2}$$

$$\cos\theta = \frac{1}{n\beta} \tag{3.3}$$

Since the refractive index varies with the altitude and the velocities of the charged particles decrease as the shower goes further into the atmosphere, also the angle of emission changes. Then, the charged particles will radiate Cherenkov photons with an angle that increases with how close the particles are to the ground, ranging from 0º to 1.5º at sea level.

These Cherenkov photons suffer little atmospheric absorption, thus being detectable at ground level. The lateral distribution of Cherenkov light is shaped as a central peak followed by a relatively flat region until 120 m, after which the Cherenkov photons density starts to decrease rapidly.

The fact that the angle of emission increases with the decrease in altitude indicates that there will be an area on the ground where the number of Cherenkov photons that arrive in that area is significantly greater than outside that region. Simple calculations show that this area is a circular region with a radius of approximately 120m. Figure 3.4 analysis the emission angle and radius at ground level of the Cherenkov photons as a function of the altitude of emission in the case of a 1 TeV muon.

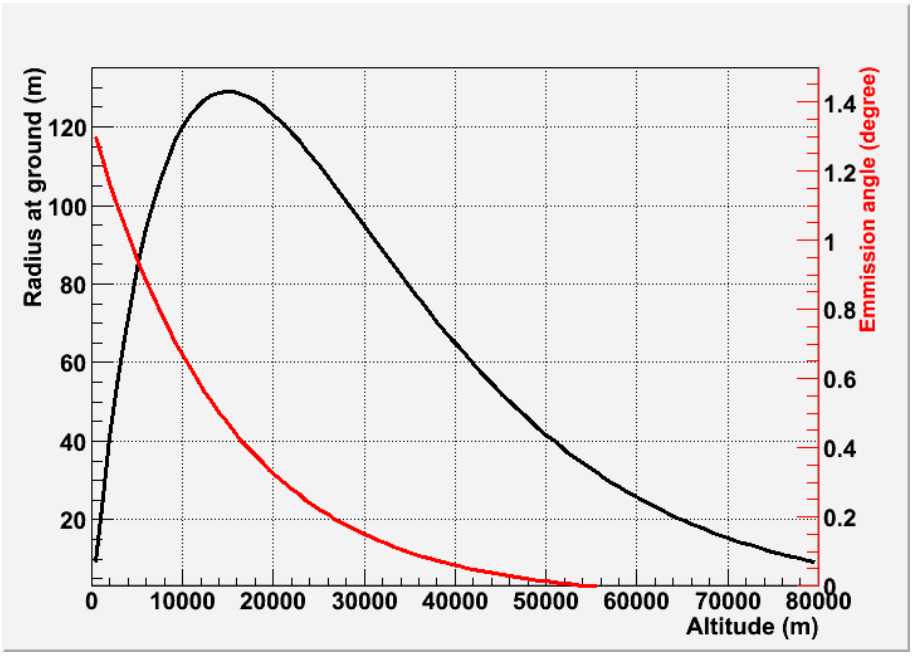

Figure 3.4: Cherenkov pool analysis as a function of altitude

3.3 Simulation

To test the proposed method, simulations of the EAS were performed using CORSIKA v6.501 [20]. CORSIKA stands for Cosmic Ray Simulations for Kascade and is a Monte Carlo program used to simulate extensive air showers initiated by high energies cosmic particles. It was developed at Karlsruhe, Germany for the Kaskade experiment.

3.3.1 Option used

The models used are the QGSJET 01C for the high energy hadronic interactions and GHEISHA 2002d for the low energy hadronic interactions. Also, the CERENKOV with emission angle depending on the wavelength and the CEFFIC options were selected.

The QGSJET option is the Quark Gluon String model with JETs, which was developed to describe high-energy hadronic interactions using the quasi-eikonal Pomeron parametrization for the elastic hadron-nucleon scattering amplitude, while the hadronization process is treated in the quark gluon string model.

GEISHA is the Gamma Hadron Electron Interaction Shower code. It is used to calculate the elastic and inelastic cross-sections of hadrons below 80 GeV in air and their interaction and particle production.

The CERENKOV option allows the simulation of Cherenkov radiation from charged particles that fulfill the condition v > c/n. The dependence of the emission angle on the wavelenght is activated with the CERWLEN option. Shorter wavelengths photons result in larger Cherenkov cone opening angles.

The CEFFIC option introduces the absorption of Cherenkov photons by the atmosphere, using data tables that contain the information of this effect as a function of the wavelength of the photons.

3.3.2 Simulated particles

For the purpose of this work, several γ and proton showers were generated with differential index of -2.49 and -2.74, respectively. In both cases, the direction of the primary particles varied in each event, as well as the core position. While the direction ranged from vertical to an inclination of 30°, the core position was simulated inside a square of 120 m side centered at the centre of the telescopes configuration (discussed further ahead).

Three different sets of simulations were performed. For the first, a hundred showers were simulated for each of the following energies: 800 GeV, 1 TeV, 1.5 TeV, 2 TeV and 3 TeV γ-ray showers and 2.5 TeV, 5 TeV and 7.5 TeV proton showers. In the second and third, a thousand γ and a thousand proton showers were generated, for each, with the energy of the primaries being determined by the energy spectrum power-laws, using an energy range of 1 TeV to 10 TeV.

Chapter 4

GAW Project

The Gamma Air Watch (GAW) project is a proposed experiment in the field of Very High Energy Gamma Rays that will begin construction in the second semester of 2007 [21]. It is a path-finder experiment in the sense that it will test the feasibility of a new generation of IACTs that combine high flux sensitivity with large fields of view. The main differences between the existing and planned ground-based Cherenkov telescopes are the optical system which will use a Fresnel refractive lens as light collector and the use of detectors in a single photoelectron counting mode instead of the typical charge integration one.

GAW will have two phases of operation. In Phase I only one telescope will be operational and tests will be performed by observing the Crab nebula between on axis and up to 12º off-axis. Furthermore, it will also be able to monitor the activity of flaring Blazars and make source detection experiments in the central regions of the Galaxy. In Phase II, GAW will consist of three telescopes and be used to make dark matter detection experiments in the central region of the Milky Way and perform a sky-survey in a region of 360°x24°.

The use of a Fresnel refractive lens will allow a FoV of 6°x6° when using a small set of photomultipliers in a first stage, and a total FoV of 24°x24° when used with the total planned number of photomultipliers.

4.1 Proposed fields of study

GAW will try to study many phenomena that occur in our Universe. In Phase I it will concentrate on Ultra-High Energy Photons from Blazars, SuperNova Remnants and Gamma Ray Bursts, Microquasars and also perform a follow-up of EGRET, AGILE and GLAST sources. In Phase II the main goals are the study of Dark Matter Annihilation in the Milky Way Galaxy, search for Nearby Earth-size Dark Matter Micro-Halos, detect Dark Matter from Intermediate-Mass Black Holes and perform an extensive survey of the sky.

4.1.1 Ultra-High Energy Photons from Blazars, SuperNova Remnants, Gamma Ray Bursts and Microquasars

Among the known sources that emit γ-rays are Blazars, SuperNovaRemnants (SNRs), Gamma Ray Bursts (GRBs) and Microquasars.

Blazars

Blazars are highly variable and very compact energy sources. They belong to the group of Active Galactic Nuclei (AGN), being associated to a supermassive black hole in the centre of a host galaxy.

A Blazar consists of an accretion disk of the order of the miliparsec inside a torus of several parsecs, that stand around the supermassive black hole and also a pair of relativistic jets perpendicular to the disk. A schematics can be seen in fig. 4.1.

Figure 4.1: Blazar [22]

Blazars are sustained by materials that fall onto the black hole. The accretion disk is formed by the captured gasses, dusts and some times stars, generating in the process enormous amounts of energy that are released in the form of photons, electrons, protons and other particles. The torus contains a hot gas formed by regions of bigger density that absorb and then re-emit energy from regions closer to the black hole.

The pair of relativistic jets behaves as a very energetic plasma, where highly energetic photons and other particles interact between themselves and the strong magnetic field. The combination of the strong magnetic fields and power winds from the accretion disk and the torus shape the plasma into collimated jets that can extend as far as many tens of kiloparsecs.

Current models predict two components in the energy spectrum of Blazars. One of low energy x-rays with energies up to 100 KeV due to Synchrotron Radiation of relativistic electrons, and high energy γ-rays up to a few TeV normally credited to Inverse Compton Scattering of the same population of electrons.

SNRs

A SuperNova Remnant is a structure that results from the gigantic explosion that occurs when a star goes supernova. It is limited by a shock wave that expands and consists of the materials that are ejected in the explosion and interstellar materials that it sweeps in its way.

The explosion expels much or all of the stellar material that, when colliding with the interstellar gas, forms a shock wave that can heat the gas to temperatures around 10 million Kelvin and form a plasma. The fastly accelerated electrons are the main responsibles for the high energy emissions in these objects as they lead to the production of highly energetic radiation through various mechanisms such as the decay of π^0 produced by hadronic collisions, Inverse Compton Scattering of electrons or non-thermal bremsstrahlung.

GRBs

Gamma Ray Bursts are the most luminous known events in the Universe since the Big Bang. They are flashes of γ-rays, that come from apparently random locations in space at also random times. These flashes can last from miliseconds to several minutes and are normally followed by an emission on higher wavelengths.

The distribution of the GRBs shows two peaks, one for GRBs of about 0.3 seconds known as short GRBs and another one at about 30 seconds, called long GRBs. Typically, each flash of γ-rays corresponds to an instantaneous energy release of an extreme amount of energy in the order of 10^{51}-10^{52} ergs.

Microquasars

Microquasars are compact accretion objects in binary X-rays systems with non-thermal radio emissions. While these systems closely resemble compact AGNs, there are some notorious differences. Instead of a super massive black hole, Microquasars are sustained by a companion star that provides the mass that accretes into the compact object.

The relativistic particles in the jets travel through strong photon and matter fields, thus being good candidates for the production of γ-rays. To explain the Very High Energy radiation, two different models have been proposed: the leptonic model and the hadronic model. Since both models predict emissions in the order of the TeV, GAW is expected to observe these types of structures, hopefully allowing some conclusions to be made.

4.1.2 Dark Matter

The new generation of IACTs is expected to provide information about Dark Matter (DM) in the universe, with the main research topics in GAW being DM annihilation in the Milky Way Galaxy, the search for Nearby Earth-size Dark Matter Micro-Halos and the detection of DM from Intermediate-Mass Black Holes.

Dark Matter annihilation in the Milky Way Galaxy

The favourite site for detection of Dark Matter annihilation, currently, is the central region of the Milky Way, where the highest density is and therefore also the highest flux. However, the Galactic Centre is a very crowed region of Gamma emitters to which one must add the high background due to difuse galactic γ-ray emission.

The problem of searching in regions far away form the Centre is fast decrease of the annihilation flux. To compensate this, a very large FoV Cherenkov telescope has to be used in order to build the requires signal-to-noise ration needed. While GLAST is expected to be able to measure DM annihilation away from the Galactic Centre up to 300 GeV, GAW should be able to complement the study with its sensitivity up to 30 TeV and a threshold of 700 GeV.

Search for Nearby Earth-size Dark Matter Micro-Halos

Micro-halos are supposed to be the first collapsed structures formed in the Universe that would have survived until now due to its high concentration of matter. With masses similar to the Earth and a typical size of about the Solar System, they should be located within more massive DM halos. The Milky Way should contain thousands of them, and the extreme proximity should enable its detectability. Recent simulation results have shown the possible existence of these structures.

To locate these microhalos, a large portion of the sky has to be studied as its positions are not known. A large FoV is then essential, making GAW the most capable instrument for its detection.

Dark Matter detection from Intermediate-Mass Black Holes

Intermediate-Mass black holes have masses around 100 to 10^6 solar masses. For typical neutralino properties, it has been shown that these balck holes can be bright γ-ray sources.

Both GLAST and GAW are expected to detect these structures with a combined energy range up to 30 TeV, covering the emission of High and Very High Energy γ-rays.

4.1.3 Extensive sky survey

The main advantage of GAW in respect to the other IACTs that are currently working or planned for the near future is its large FoV. As the detection of Gamma-ray sources is now dependant on the serendipity search capability of the detectors, GAW will then be the most promising source detector.

The proposed GAW survey will cover a significant portion of the sky as a two year search will be performed in which it will look at an area of 24°x360° (20% of all the sky). This study will include part of the Galactic Disk and a big fraction of the extragalactic sky.

In a first stage, where only a FoV of 6°x6° is available, GAW will do a follow-up on known sources, particularly on the most recent ones at the time discovered by GLAST and AGILE.

4.2 GAW configuration and location

GAW will be composed by three identical telescopes disposed at the vertexes of an approximately equilateral triangle of 80 m side as seen in figure 4.2. Each telescope will have a focal length of 2.56 m, with the refractive lens of 2.13 m diameter at its end.

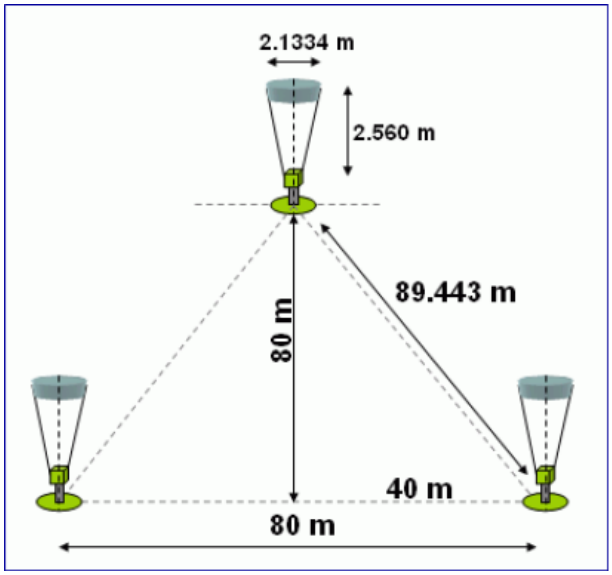

Figure 4.2: GAW telescope configuration [23]

The telescopes will be built at the Spanish-German Astronomical Centre at Calar Alto, which is located in the Sierra de Los Filabres in Almeria, Spain. At an altitude of 2168 m, this observatory is one of the best in Europe with excellent atmospheric conditions due to its low light pollution and high cloudless night numbers. Also, the site has already local facilities and infrastructure needed for GAW.

4.3 Optics

The GAW light collector is a Fresnel lens with a 2.13 m diameter, a focal length of 2.55 m and a standard thickness of 3.2 mm. The lens will be made of UltraViolet transmitting acrylic with a nominal transmittance of about 95% from 300 nm to the near infrared. Since this material has a high transmittance and a small refraction index derivative at low wavelength, the chromatic aberrations effects are reduced. The lens design is optimized to have a very uniform spatial resolution up to 30° at the wavelength of maximum intensity of the Cherenkov light ($\lambda \approx 360$ nm).

The lens is composed of a central core diameter of 50.8 cm, around of which there are two circles of petals. The inner circle extends the radius another 40.6 cm, as well as the outer circle. The inner centre will be composed of 12 petals, whereas the outer ring will have 20 pieces. The pieces will be held together by a spider support. Figure 4.3 is a schematics of the lens.

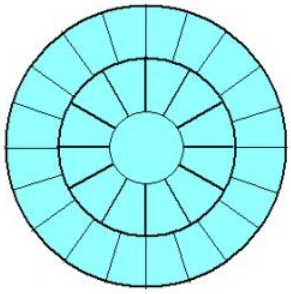

Figure 4.3: Lens design [24]

A simulation was performed to study the lens transmission as a function of the angle of incidence with the results shown in figure 4.4. The blue curve was obtained using the nominal value of the absorption length for the UltraViolet transmitting acrylic material. The red curve, for comparison, shows the case setting to infinite the absorption length of the lens material.

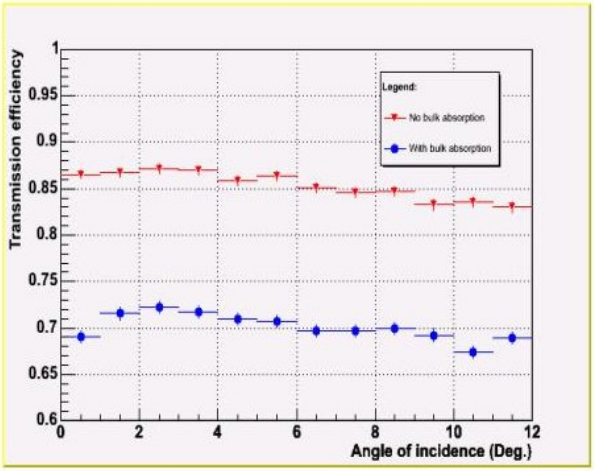

Figure 4.4: Lens transmission efficiency vs incidence angle [24]

4.4 Light Guides

The large dead area of the photomultipliers (PMTs) used as focal surface detectors induces a low geometrical efficiency that can be corrected with the use of Light Guides. These are associated to each PMT pixel allowing a geometrical efficiency factor close to 100 $\%$.

Each Light Guide consists of a UV transparent pyramidal frustum 40 mm tall with squared surfaces at the top and bottom. The smaller area on the bottom is closely the same as the area of one pixel of the PMT. The large squared area on the top has a size of 3.9 mm. The Light Guides are glued on the top using a single foil of 1 mm thickness and 31x31 mm^2 of surface that corresponds to a compact ensemble of 64 Light Guides. Each ensemble is optically coupled to a PMT. An ensemble is shown in figure 4.5.

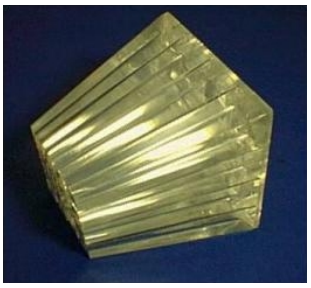

Figure 4.5: Ensemble of Light Guides [24]

The transmission mode of the Light Guides is total reflection from top to bottom. They are molded using a high UV transmitting polymer with a refractive index of 1.49 (at 360 nm).

4.5 Electronic system

A large number of active channels will constitute the focal surface of the GAW telescope making it, basically, a large UV sensitive digital camera with high resolution imaging capability.

The GAW electronics is based on single photoelectron counting method (front-end) and free running method (data taking and read-out). The single photoelectron counting method is used to measure the number of output pulses, from the photo-sensors, that correspond to incident photons. A small pixel size is then needed to minimize the probability of photoelectrons pile-up within shorter intervals than the Gate Time Unit (GTU).

The free running method uses cycle memories to continuously store system and ancillary data at a predetermined sampling rate. When a specialized trigger stops the sampling procedure, data is recovered from the memories and is ready to be transferred to a mass memory.

Because of the large number of channels and the limited amount of space available, a compact design with minimal distance between the detector sensors and the front-end electronics is required. A completely modular system with minimal cabling and self-triggering capabilities will then be implemented.

4.5.1 Front-End Electronics

A front-end electronics is used to preamplify the signals coming from each of the anodes of the MultiAnode PhotoMiltiplier Tubes (MAPMTs, the detector sensors used), discriminate them with a programmable threshold and store the resulting digital count in the cycle memories. A high-speed linear amplifier is

connected to each anode out while an adjustable threshold discriminator shapes the amplified pulse to a standard logic level. At every GTU, the signal is sampled and candidate to be recorded.

4.5.2 Read-Out

Each PMT works independently of the front-end and data storage in the cyclic memories, with interconnections with adjacent MAPMTs for trigger generation. This allows the reproduction of units in a modular way. Every GTU, the positions number and arrival time of the detected photoelectrons are recorded separately in the cyclic memories.

Without a trigger signal, the memory will be continuously written, updating the information already stored. When a specialized trigger signal is received, the writing operation stops and the memories are read out for an appropriate time unit length. The controller system manages the addressing of the memories and governs the writing and reading operations.

4.5.3 Trigger and Remote Control Electronics

Due to the very low level of noise per pixel ($\approx$0.01 photoelectrons/pixel/GTU), a typical Cherenkov image on the focal surface can be distinguished from accidental noises. Each of the trigger configuration register, located on the units, can be set by remote control command. To suppress random coincidence due to the single event rate, majority logic associated to positions and local density is implemented.

A trigger is generated when the conditions set on the configuration registers are met. To reduce the rate of fake triggers that are originated by the diffuse night-sky light, a second level trigger will also be implemented. This trigger will perform a coincidence of the three telescopes in a time-window of a few hundreds of nanosecond.

4.6 Focal Surface Detector Configuration

The GAW focal surface detector is formed by an array of MultiAnode PhotoMultiplier Tubes inserted in an electronic instrumentation UVIScope (Ultra Violet Imaging Scope) capable of conditioning, acquiring and processing a great number of high speed and high rate pulse signals.

To quickly obtain a compact detection plane and assure a closed tubes assembling, the basic and repeatable parts of the UVIScope instrumentation have been conceived in a modular style with two units: a Fronte-End Brick unit (FEBrick) and a Programmable Data Acquisition unit (ProDAcq).

4.6.1 MAPMT

The MAPMT used in the GAW focal surface detector has 64 anodes arranged in an 8x8 matrix with the tube section measuring 25.7x25.7 mm^2 with length of 33 mm and weight of 30 g.

The tube is equipped with a bialkali photocathode and a UV-transmitting window 0.8 mm thick, that will ensure a good quantum efficiency for wavelengths longer than 300 nm with a peak of 20$\%$ at 420 nm. Also, the device has a Metal Channel Dynode structure with 12 stages, providing a gain of the order of 3x10^5 for a 0.8 kV applied voltage.

4.6.2 FEBrick

The FEBrick is a modular front-end unit that works in Single Photon counting mode. It was conceived for a single MAPMT and provides a low power active high voltage divider. It is located at the bottom of the MAPMT as an appendix of identical section with a length of 85 mm. Straight connection of the unit on the bottom of the MAPMT allows the preservation of the anodic signals.

The FEBrick returns both digital photon location of the cathode surface and analog information of the total charge detected from MAPMT. It is composed of a tube insertion socket, a low power active high voltage divider, 64 anodic channels that operate in Single Photon Detection, 1 dynodic channel that operates as charge integrator and a digital reading temperature sensor.

4.6.3 ProDAcq

The ProDAcq units are inserted bellow the FEBricks, with a blackplane performing the connection between them. The signals detected by the FEBrick units are sampled by the ProDAcq units and then acquired according with suitable and flexible user algorithms.

Each unit is internally managed by a reprogrammable FPGA. The digital signals may be sampled up to 400 MHz and recorded inside three memory banks for 192 Kword storage capacities. The input analog signal may be sampled fastly and accurately according with the wiring combination of two ADC converters respectively running in AC and DC mode.

Chapter 5

Shower Characterization

The methods to reconstruct air showers are usually 2D methods that work with the image of the projection of the air shower on each of the telescopes. These images are constructed using the pixels that report counts of Cherenkov photons and are then analyzed as described before.

This work intends to further develop the methods used for air showers reconstruction by taking advantage of the improved Cherenkov detectors. In these new Cherenkov detectors, the number of pixels is large and therefore each pixel has its own well-defined direction, defined by two different angles θ and ϕ. The first angle is the angle made by the Cherenkov photon direction and the vertical axis, while the second one is the angle between the projection of the direction on the XY plane and the X axis. A geometrical representation can be seen on figure 5.1.

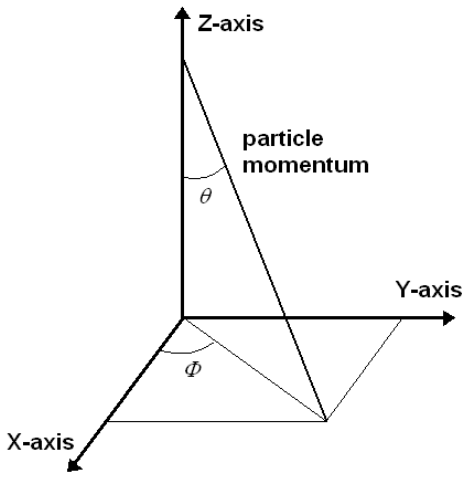

Figure 5.1: Geometrical description of the particle direction

In the basis for these types of methods, it is assumed that the shower can be viewed as a cone with the major axis coinciding with the primary particle direction. As such, the arriving particles would have been emitted on the axis, or near it, having conical symmetry. With these assumptions, one can easily imagine that each of the pixels that were hit by Cherenkov photons actually connects the telescope to some point in the shower axis.

The assumption that the Cherenkov Photons all came from the Primary particle direction is a strong one, but one can argue that if we consider a shower with a large number of Cherenkov Photons emitted, they will come mostly of a region close to the axis as the γ-ray air showers are very narrow and focused.

The algorithm used in the 3D reconstruction will then have to be able to choose, from all of the pixels, those that point to the axis and "neglect" the ones that do not.

As it was said, to each pixel we associate a specific direction that corresponds to the one defined by the values of θ and ϕ at the centre of the pixel. This definition produces a slight error for each photon, as the angles of arrival could have been any that would fit in that pixel. For example, in the GAW case, each pixel measures 0.1º per 0.1º. In this case, each γ could have arrived with $\theta_i \pm 0.05$º and $\phi_i \pm 0.05$º.

The error that comes from assuming the central angles of each pixel is very small, which can be explained with simple trigonometry. If we consider an error of 0.05º for θ, to have an error of 1 m in the reconstructed point, the detector would have to distance itself about 1 km from the reconstructed point ($\approx 1\text{m}/tg(0.05^\circ)$).

With the developed 3D method we foresee a significant improvement on the results of the determination of the air shower direction as well as the location of the core. Furthermore, we expect to gain enough sensitivity to rebuild the portions of the shower seen by the telescopes which can in turn help to a better understanding of the spatial distribution of Cherenkov photon on Gamma-ray Showers.

5.1 New Discrimination Variables

The use of 3D methods provides new and valuable information about the shower that was seen by the telescopes. This is due to the fact that we use all the information available and actually perform an approximated reconstruction of the shower itself.

It is with this reason that one can try to find some new variables to distinguish Gamma-ray showers from Proton ones. Two variables can be used to characterize each Cherenkov photons path in respect to the main axis (cf. fig. 5.2):

- the emission angle of each Cherenkov Photon (α);
- the impact parameter (b).

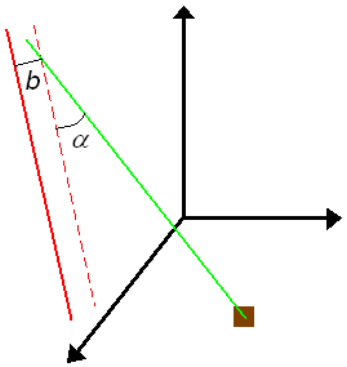

Figure 5.2: Definition of the new discrimination variables

The angle of emission is defined as the angle between the main shower axis and the direction of the arriving Cherenkov Photon. As we know, the Cherenkov emission is very collimated which means that the angles of emission are generally very small, with a peak on 1.5º.

The impact parameter is the distance between the emission point and the main shower axis. This is calculated as the point in the reconstructed photon path that is closest to the main shower axis, so long as this point is above the ground. The cases in which the calculated point is bellow ground occur when the Cherenkov photon was emitted from a secondary particle far away from the main axis. These cases

will be stacked all together and we will say that their impact parameter was the distance detector-core, as this is the maximum distance above ground.

This solution, although not a physical one, has proven itself to be very helpful when it comes to distinguish between γ-ray or Proton showers as it is a measure of how wide the shower was.

It is commonly known that there are several differences between both types of showers that are in study here. We will name only those that will help us determine what type of shower we have given images from our Cherenkov Telescopes.

The main difference with which we work on is that Proton showers are much wider then γ-ray showers. This is due to the fact that a charged shower produces secondary particles that spread in every direction while γ-ray showers produce electron-positron pairs with very small angles in respect to the primary particle direction.

In our case, this translates in the fact that we will have a bigger percentage of photons that come from regions of the shower further away of the main axis in the case of Protons, while in the case of γ-rays this percentage should be smaller. As we have seen, this would mean that these photons will stack in the maximum distance, making this peak more prominent.

5.1.1 Angle α

As for α, since γ-rays are very narrow, we expect to see a well-defined peak in small angles. Also, we know that there is a correspondence between the height of emission and the angle of emission which implies also a relation between the angle of emission and the distance in the ground from the detector to the shower core. Hence, for different distances we expect also different values for the peak.

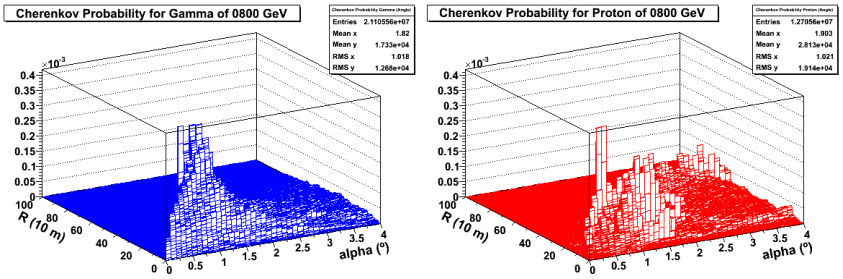

Figure 5.3: Gamma-ray and Proton comparison of α at 800 GeV

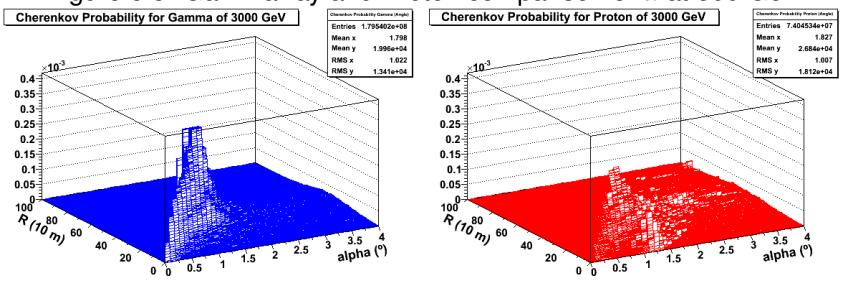

Figure 5.4: Gamma-ray and Proton comparison of α at 3000 GeV

In the Proton case we have Cherenkov photons arriving from every direction so, while we still expect to see a peak at values close to that of the γ-rays, these should be smaller and wider.

To confirm these expectations several simulations were performed using Corsika to simulate the air showers. Here we present the cases of Proton and γ-ray showers in the energy of 800 GeV and 3 TeV

each. All simulations were performed with θ and ϕ equal to zero. To have a better understanding of how these variables work, all the arriving Cherenkov photons were considered.

Beginning with the analysis of α, we have on figures 5.3 and 5.4 the Cherenkov probability as a function of R (which is the distance between the arriving point of each particle and the shower core) and α. In blue we will have γ-ray induced showers and in red Protons showers.

Analysing these plots it is clear that there are significant differences between Gamma and Proton showers. The distributions of the Gamma-ray showers appear to be very well-defined, peaking at 1.5º as it was expected. On the other hand, the Proton showers distributions appear more irregular. There does not seem to exist a peak in these cases although one can say that there is definitely a relative maximum value around 1º - 1.5º

Also, if we compare the images of 800 GeV with those of 3000 GeV, we can see that in the case of Gamma-rays, the higher the energy the more well-defined the peak is. In the cases shown above, the 3000 GeV peak is narrower and smoother than the 800 GeV one. One reason for this might be the larger statistic available for the 3000 GeV case.

In the protons, we have that the 800 GeV distribution has higher values than that of the 3000 GeV case. This might indicate that we have higher values of α that do not appear in the plot. Since we know that the higher the energy the wider the Proton showers are, it seems to make sense the existence of higher values of α. However, since the purpose of this work is primarily to identify γ-rays, only the good regions for γ events were studied.

5.1.2 The impact parameter

For the impact parameter we can follow the same line of study and the obtained results can be seen on figures 5.5 and 5.6.

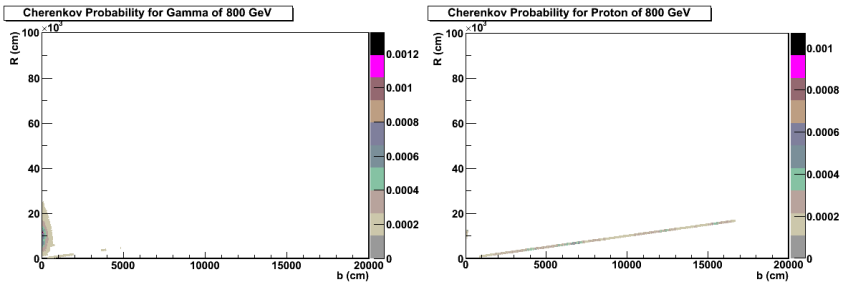

Figure 5.5: Gamma-ray and Proton comparison of b at 800 GeV

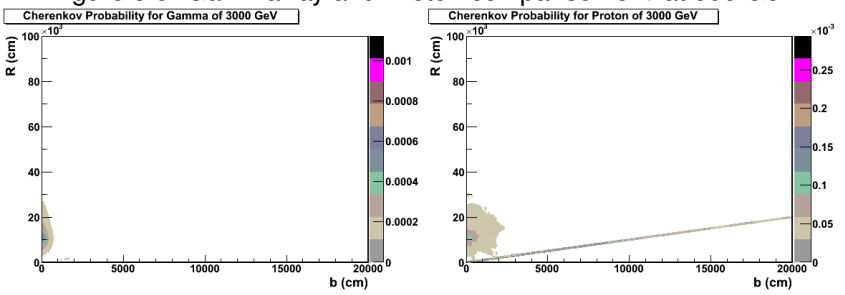

Figure 5.6: Gamma-ray and Proton comparison of b at 3000 GeV

The first thing one should notice in these plots is the straight "lines" that appear on all of them (although they are smaller and more difficult to see in the γ cases). These lines are the ones that

represent b equal to R. As it was already discussed it is natural that these lines appear more prominently in the Proton cases than in the γ-ray cases.

Once again, the distributions for the γ-ray showers appear very organized and are restricted to a small area corresponding to small impact parameters. This is in agreement with what was expected, as most of the Cherenkov photons are emitted near the main shower axis.

Otherwise, the Proton showers distributions are not as regular, and it is clear that the line already mentioned "masks" some part of the plots due to its importance. In the 800 GeV case this is clear as it is the only part seen of the graph, while in the 3000 GeV case it has a smaller part of the plot but still is easily seen.

5.2 Study of the new variables at fixed radius

A more detailed study was performed having in mind that our detectors will be at some distance from the shower core. In order to have better statistics, a ring of one meter of internal radius was considered around the presented distance. This clearly gives more statistic to higher distances which compensates, in some way, the fact that the number of Cherenkov photons per square meter decreases with the distance.

As such, we used the data presented above to study these new variables at fixed distances ($10m$, $20m$, $70m$ and $150m$).

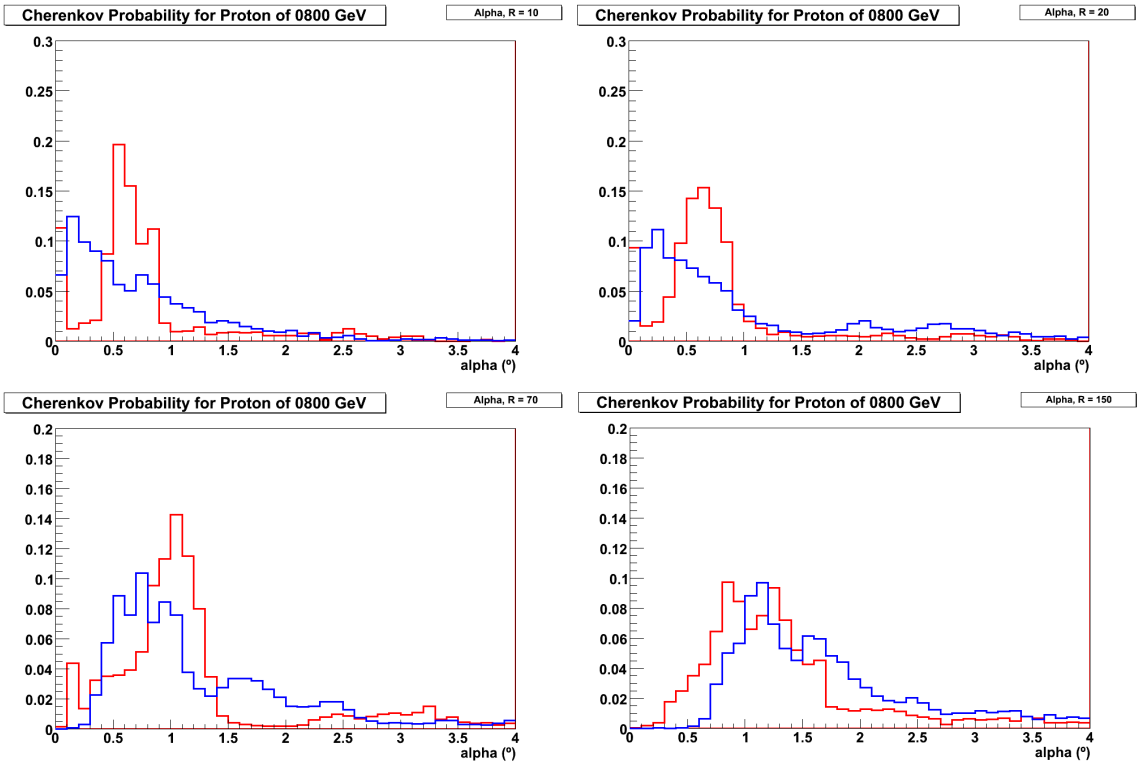

Figure 5.7: Gamma-ray and Proton comparison of α at 800 GeV for different radius

5.2.1 Angle α

Starting with α, we have in figure 5.7 the plots for each of the already referred radius for 800 GeV and in figure 5.8 for 3000 GeV. These two figures demonstrate that for small distances between the core position and the detector, there is a significant difference in what concerns the location of the peak of the α distribution as for the γ-ray Showers it is located near 0º and for the Proton Showers around 1º.

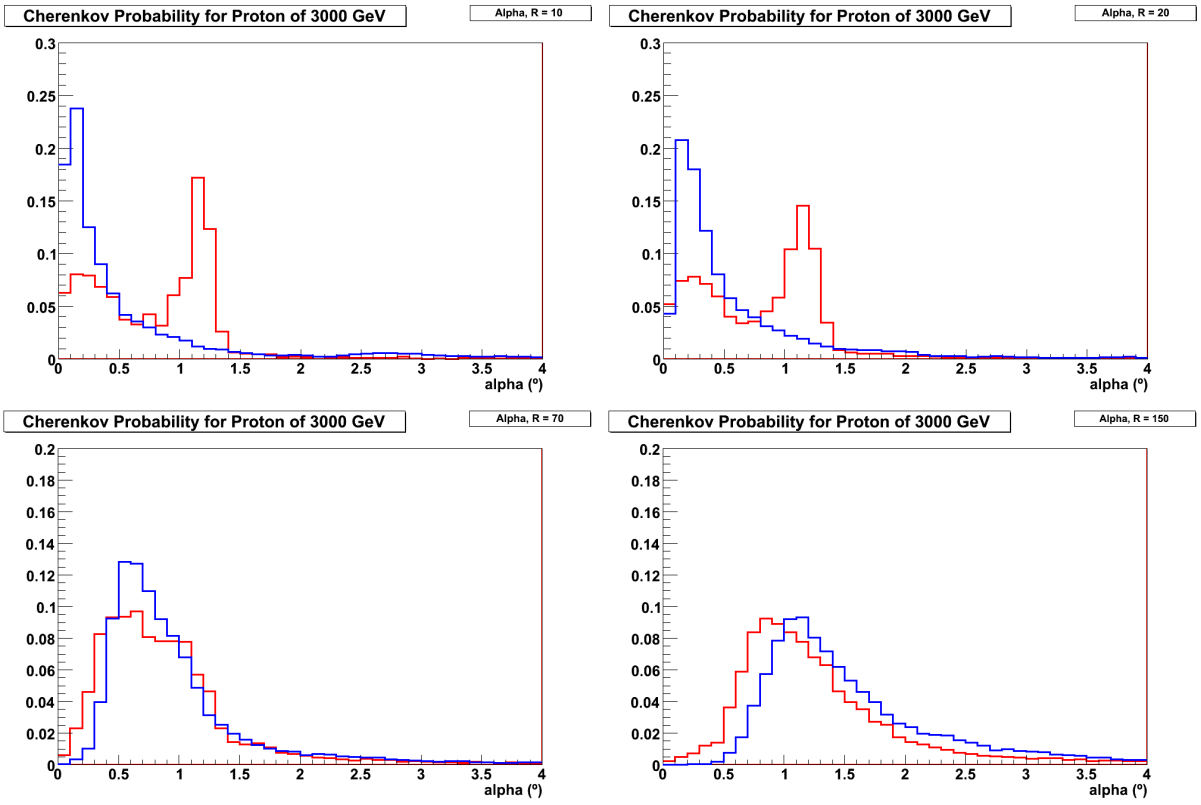

Figure 5.8: Gamma-ray and Proton comparison of α at 3000 GeV for different radius

With the increase in distance, it is clear the peaks get closer and, at about 70m, they exchange orders, as the Proton peak appears at lower α than the Gamma-ray peak. From the 70m to the maximum studied (150m), the peaks closely resemble each other, thus becoming difficult to distinguish them.

Some differences can be seen by comparing both energies. For the Gamma-ray showers, our main concern, these differences are simply the better definition of the peaks due to better statistic. In the Proton case, the peak location for small radius gets higher, going from 0.7º at 800 GeV to 1.2º at 3000 GeV. This is due to the increase in the wideness and length of the shower, with particles being created at lower altitudes with bigger angles.

5.2.2 Impact parameter

In figures 5.9 and 5.10, it is shown the evolution of the distribution curves of the impact parameter for 800 GeV and 3000 GeV, respectively, with the increase in distance.

In these figures it becomes clear that the increase in the radius allows a better separation between the Proton and Gamma-ray curves as the Proton curves show the referred pile-up where b equals R. On the other hand, Gamma-ray showers have a clear peak at low values of b showing, nonetheless, a small peak (for big distances) also where b equals R.

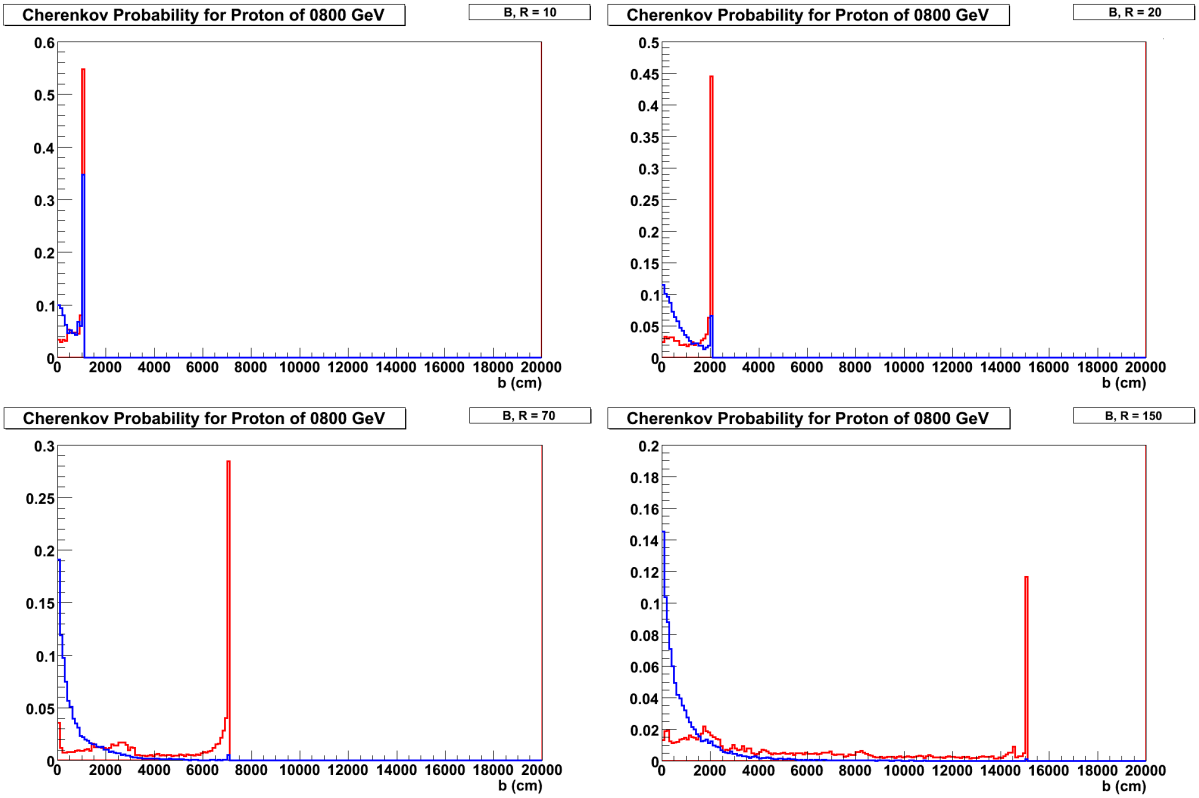

Figure 5.9: Gamma-ray and Proton comparison of b at 800 GeV for different radius

For small distances it is fairly secure to conclude that the impact parameter will not provide much information about the nature of the shower, while for big distances the differences seem enough to separate Gamma-rays from Protons.

The increase in the energy of the primary particle provides more information about the shower, but in the case of the Protons, this means that the significance of the peak at high b is lowered. However, it does not seem that it will be low enough to be confused with the Gamma-ray curves.

5.3 Overall variables evaluation

The information presented in the sections before allows some conclusions to be made in what regards the usefulness of the introduced variables in the separation of Gamma-ray induced showers from Proton induced ones.

As it was shown, each variable has a well-defined region of influence, where the spectras are very different for each case. For α, the variable appears to have a very good discrimination power at small radius, while the impact parameter's "good" range is at medium and high radius.

In respect to the dependence of these variables in Energy, small differences can be seen. However, these differences can be considered negligible as the general differences between Gammas and Protons are maintained, becoming more noticeable as the energy is increased.

Together, both variables cover all the studied distances, which are fairly the distances from which the telescopes will "see" the showers. Therefore, these variables look solid enough to proceed with a more detailed study, which is done in Chapter 7.

The main difficulty now is that the calculation of these variables can only be done with the knowledge

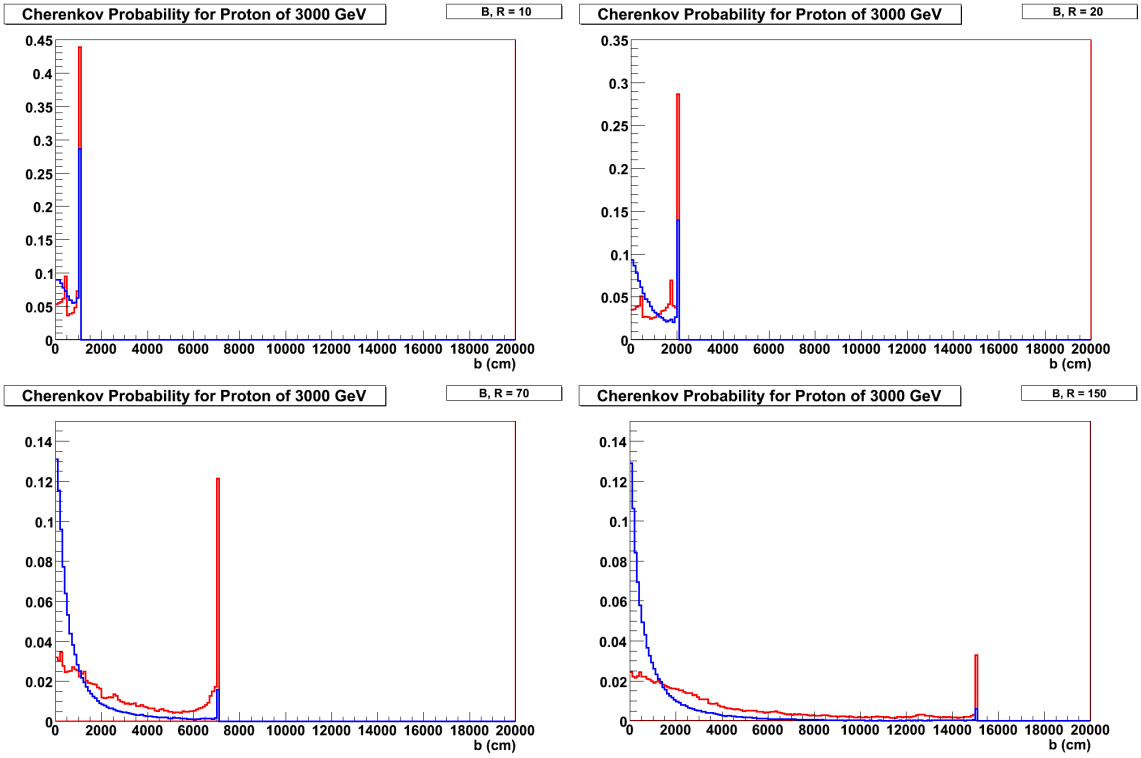

Figure 5.10: Gamma-ray and Proton comparison of b at 3000 GeV for different radius

of the shower direction and the shower core location.

Chapter 6

Shower Geometrical Reconstruction

A 3D method was developed to reconstruct air showers. As input, the method needs to receive a set of images that represent the directions of arrival of each Cherenkov photon that hits a specific detector.

The method consists of two different analyzes, one to determine a first guess of the core location and the shower direction and a second part that is iterative to improve the initial guess.

It is important to discuss that in this method, each detector is treated as a punctual detector and so, every Cherenkov photon from that detector is assumed to have arrived at that exact point, which will be considered the centre of the detector. This is an approximated solution as the information available for each photon does not include the position of arrival. As such, what we have is directions in space, passing by fixed points in the ground plane.

6.1 Calculation of the Initial Guess

For every pair of directions that belong to different detectors and whose θ differ from one another not more than 1°, excluding the exact parallel ones, the point in space that is closest to the two lines is calculated . This can be done by firstly defining the two lines as shown in equations 6.1 and 6.2, where $det1$ and $det2$ are the detectors positions and $dir1$ and $dir2$ are the directions of two different photons (cf. fig. 6.1).

$$P \in \vec{det}_1 + t \cdot \vec{dir}_1 = m \tag{6.1}$$

$$Q \in \vec{det}_2 + s \cdot \vec{dir}_2 = l \tag{6.2}$$

Using this definition, the points P and Q, that correspond to the points in each line that are closest to the other one, belong to the perpendicular planes of the opposite line that passes on the other point. For example, point P belongs to the perpendicular plane of line m that passes through Q, and vice versa.

With this in mind we can calculate s and t (equations 6.3 and 6.4) that give us points P and Q by using the two equalities available, one from each plane.

$$t = \frac{\vec{dir}_1 \cdot (\vec{det}_2 - \vec{det}_1) + s \cdot \vec{dir}_1 \cdot \vec{dir}_2}{\vec{dir}_1 \cdot \vec{dir}_1} \tag{6.3}$$

$$s = \frac{\vec{dir}_2 \cdot (\vec{det}_1 - \vec{det}_2) + (\frac{\vec{dir}_2 \cdot \vec{dir}_1}{\vec{dir}_1 \cdot \vec{dir}_1}) \vec{dir}_1 \cdot (\vec{det}_2 - \vec{det}_1)}{\vec{dir}_2 \cdot \vec{dir}_2 - \frac{\vec{dir}_1 \cdot \vec{dir}_2}{\vec{dir}_1 \cdot \vec{dir}_1}} \tag{6.4}$$

Having both points, the point that is closest to the two lines is simply the middle point between P and Q (cf. fig. 6.1) and is easily computed with equation 6.5.

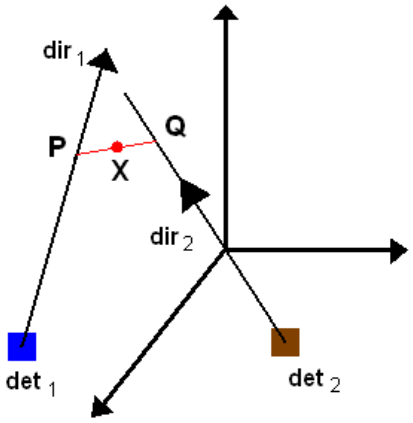

Figure 6.1: Definition of the middle distance point between the two lines (point X)

$$\vec{X} = \frac{\vec{P} + \vec{Q}}{2} \tag{6.5}$$

As some showers are very wide and can introduce some opposite directions on the telescopes, it can happen that the point determined appears to be bellow ground. Since no emission could have come from there, these points are neglected.

One consideration that has to be done is that some detectors are able to have an estimate of how many Cherenkov photons were received in each pixel, while others are only able to know if a pixel was hit by photons or not (not knowing how many they were). This clearly introduces weights to each pixel, proportional to the number of photons that hit them. In the case of the X points, the weight will be the product of the weight of each direction involved in the calculation.

Using this algorithm, a cloud of points that could roughly be interpreted as the possible points of emission of Cherenkov photons, and therefore, the points where secondary particles of the air shower passed is obtained. The distribution of these points may then help to determine the main axis of the shower as the direction of secondary particles follows, approximately, the primary particle direction.

The calculation of the first guess for the main axis is done by computing the "centre-of-mass" (CM) of the cloud of points and building the Inertia Matrix with respect to this CM. The CM is calculated using equation 6.6 where n_j is the weight of each point and N the number of points.

$$\vec{CM} = \frac{\sum_{j=1}^{N} n_j \vec{X}_j}{\sum_{i=1}^{N} n_i} \tag{6.6}$$

The Inertia Matrix (cf. 6.7) is built by, first, calculating the distance between each point and the CM, d_i, and then computing each entrance of the matrix as explained in equations 6.8. The main inertia axis is the third eigenvector, the one that corresponds to the z axis.

$$I = \begin{pmatrix} I_{xx} & I_{xy} & I_{xz} \\ I_{yx} & I_{yy} & I_{yz} \\ I_{zx} & I_{zy} & I_{zz} \end{pmatrix} \tag{6.7}$$

$$I_{xx} = \sum_{i=1}^{N} m_i(d_{iy}^2 + d_{iz}^2); \quad I_{yy} = \sum_{i=1}^{N} m_i(d_{ix}^2 + d_{iz}^2); \quad I_{zz} = \sum_{i=1}^{N} m_i(d_{ix}^2 + d_{iy}^2);$$
$$I_{xy} = I_{yx} = -\sum_{i=1}^{N} m_i d_{ix} d_{iy}; \quad I_{xz} = I_{zx} = -\sum_{i=1}^{N} m_i d_{ix} d_{iz}; \quad I_{yz} = I_{zy} = -\sum_{i=1}^{N} m_i d_{iy} d_{iz}; \tag{6.8}$$

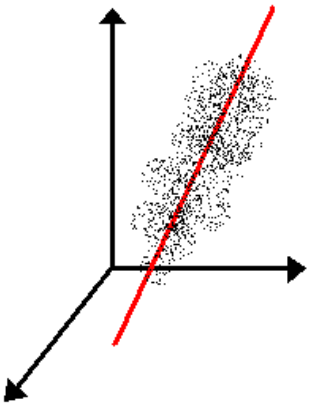

Figure 6.2: Main Inertia Axis of a set of points

In order to evade a possible bias introduced by the collocation of the telescopes, the first guess for the core position can be determined using the guess for the main axis and a point that is closely located to the real main axis. The determination of this point is done by analyzing the directions of the arriving photons at each telescope.

Each telescope has a preferential direction that can be calculated by performing an average on the directions of arrival of the photons on that detector. As was discussed, most Cherenkov photons are emitted close to the main shower axis, so these directions should point to some part of the showers path. The point that stands closest to all the directions available (one per each detector) can be considered as a point close to the real main axis position.

To calculate this point, equations 6.1-6.5 are used in which the directions are now the average from each telescope. If there are N telescopes, the number of points to calculate is $(N-1)N/2$. The average of these points gives the assumed main axis point.

Considering that the shower core location is where the primary particle would have hit the ground if it did not interact with the atmosphere, the assumed main axis point and main axis direction can be used to compute the first guess for the core position.

6.2 Iteration Phase

The method then enters an iterative phase. In this phase, the method starts by calculating the closest points between each direction in each detector and the current main axis position. Once again the equations used are those from 1 to 4, but in this case $det2$ is the current core location and $dir2$ is the current main axis. The point chosen is point P, the point that lies in the line of the direction in study that is closest to the main axis. Once again, the calculated points that are below the detector level are not admitted.

These points can be understood as the location of emission of each of the Cherenkov photons as they are the point closest to the main axis that stands in the straight line which approximates each photons path.

For each point is computed the impact parameter (distance to the main axis). To attribute a sign to the impact parameter, it is calculated for each detector the cross product between the line that unites the current core position to the detector and the current major axis (vector v). Also, the vector that unites P and Q (going from Q to P) is computed. The sign of the impact parameter is chosen in accordance with the result from the dot product between these two vectors.

An example is shown if fig. 6.3. There it can be easily seen that the cross product between QP and v has a negative value and as such the impact parameter will have a minus sign.

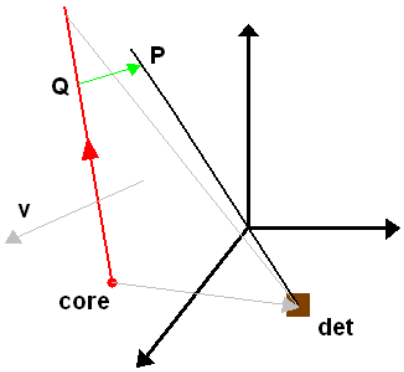

Figure 6.3: Sign of the impact parameter

This creates a set of points with associated values of impact parameters. A subset is constructed by applying a first cut-off in respect to the impact parameters. For this we have defined that the impact parameter has to be somewhere between a minimum and maximum value that change with every iteration (cut_{min} and cut_{max}), for each detector. In the first iteration, these extreme values are such that allow every point to be taken in consideration.

An average of the impact parameters ($\bar{b}$)is then calculated for each detector, and also the sigma value of the impact parameter distribution according to equation 6.9.

$$\sigma = \sqrt{\frac{\sum_N^{i=1}(b^2 - \bar{b}^2)}{N-1}} \tag{6.9}$$

Using these values, a smaller subset is created with the points whose values are between the average plus minus 3σ. For the first iteration, 3σ is used, but this is decreased every time the core location converges. The number of sigmas used at each iteration will be called $multiple$.

With this new group of points, the CM and the Inertia Matrix are then calculated and the value of the major axis is updated. Here it can be easily considered the CM to be the point that stands in the primary particle supposed path and use it and the major axis to compute the new core position.

This new core position is then compared to the previous one by calculating the distance ($dist$) between the new core and the one from the previous iteration. If the distance is more than a predefined tolerance (a good value appears to be $multiple \times 20$cm), the method has not converged yet well enough and, we simply update the cut_{min} and cut_{max} values. If the number of photons used in the detector is more than 25, a value that seems to guarantee that in the next iteration there will always be some photons inside the new cut, eq. 6.10 is used. If not, but is still bigger than 0, then eq. 6.11 is used. Otherwise, these values are set big enough so that in the next iteration all of the photons will be used.

$$cut_{min} = \bar{b} - multiple \times \sigma$$
$$cut_{max} = \bar{b} + multiple \times \sigma \tag{6.10}$$

$$cut_{min} = cut_{min} - dist/2.$$
$$cut_{max} = cut_{max} + dist/2. \tag{6.11}$$

If the core has moved less than the tolerated value, the cut_{min} and cut_{max} are also set to high values so that they do not cut out any point, while the multiple of sigma is diminished by 0.2. As a fail safe, if the method performs 100 iterations without convergence for a multiple of sigma, it proceeds as if the core had stabilized.

The iteration stops when a value of multiple of sigma equal to 1.5 is achieved and the core position moves less then the tolerated value. With this iteration process it is expected that as the multiple of sigma is diminished, the method becomes more and more precise due to the method closing in on the real main shower axis and the fact that points that came from regions further away the main shower path are cut off.

6.3 Results

Using the first set of simulated showers, the results provided by the method can be analysed as a function of the energy and the type of the primary particle. Figures 6.4 and 6.5 show the average difference between the reconstructed core position and the real core position for γ and proton showers.

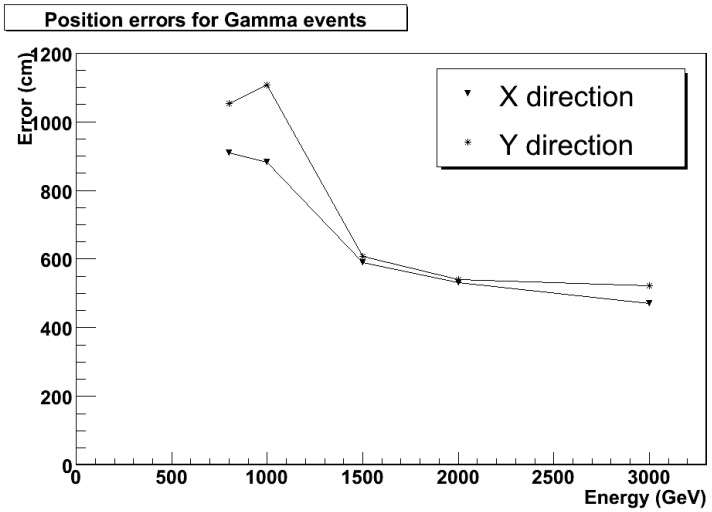

Figure 6.4: Distance between the real core location and the reconstruction core position for γ events

From these figures, some conclusions can be made regarding the method. In both cases, the results improve with the increase in the energy of the primary particle. This is expected as the method uses the particles collected in each telescope and an increase in the energy is translated in a larger number of photons.

Comparing both primaries, one can see that the errors in the proton case are roughly twice those in γ showers. The basis of this method is that the Cherenkov photons are emitted close to the shower

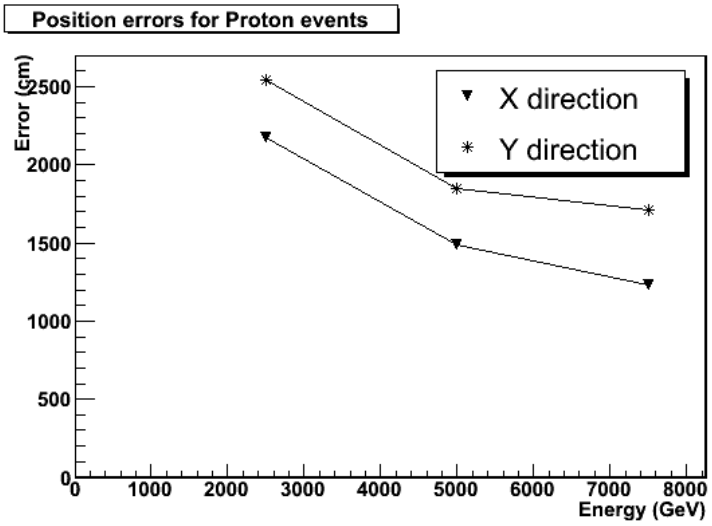

Figure 6.5: Distance between the real core location and the reconstruction core position for proton events

main axis and therefore, compact showers are better reconstructed. This explains why γ showers have smaller errors in comparison to proton showers, that are wider.

To study the reconstructed main axis, the deviation angle was analysed. This angle is defined as the angle between the reconstructed main axis and the real main axis. Figures 6.6 and 6.7 show the average deviation angle for γ and proton showers at different energies.

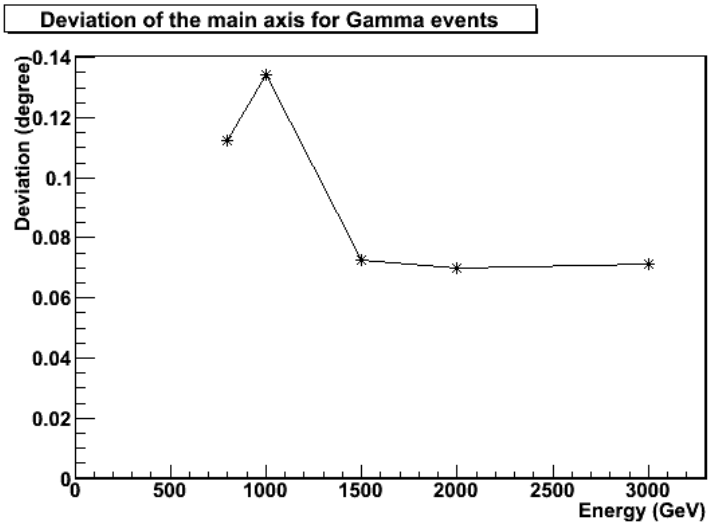

Figure 6.6: Deviation of the reconstructed main axis for γ events

Once again these figures show better results for γ events than for proton showers. There does not seem to be a significant improvement with the increase in energy as the deviation angle is already very small (around 0.1° for γ and 0.3° for protons).

Figures 6.8 and 6.9 show the reconstruction of a γ event and a proton event, respectively. The lines in red represent the reconstructed main shower axis passing through the reconstructed shower core position. The points in the plots are the closest points to the shower main axis from each arriving direction which, as it was already explained, are approximately the points of emission of the Cherenkov

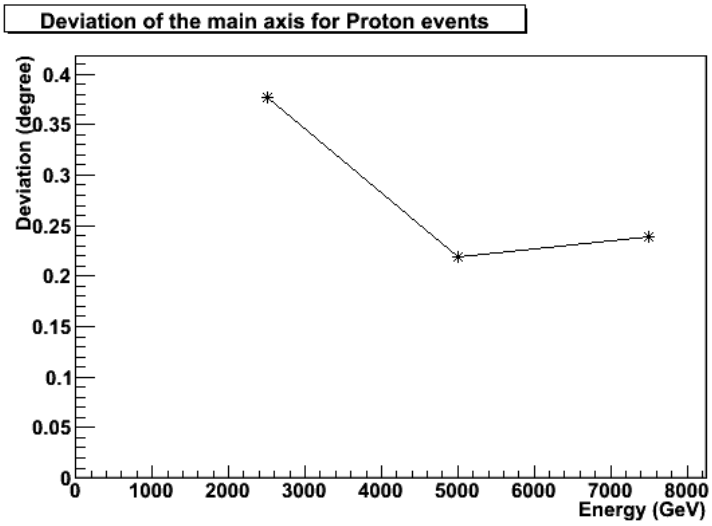

Figure 6.7: Deviation of the reconstructed main axis for proton events

photons. The colors of the points change with their height (z).

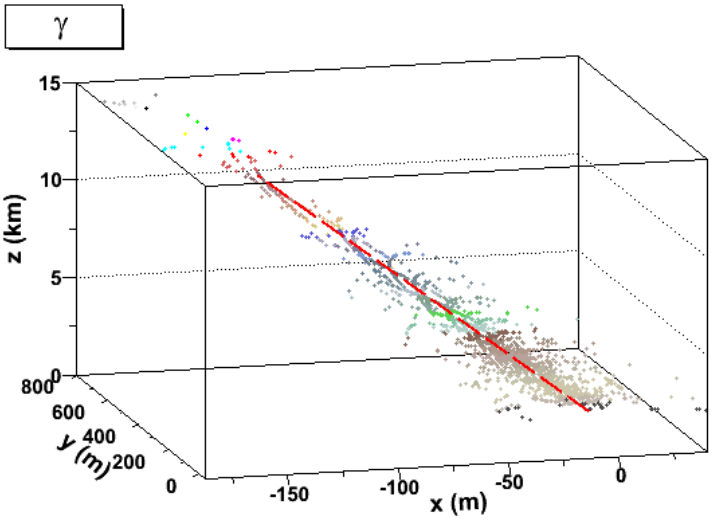

Figure 6.8: 3D reconstruction of a γ event

Also, a study of the average error for the core position as a function of the location of the real core position was performed using the third set of simulated showers. Figures 6.10 and 6.11 show the results from this study, where the telescope positions are signaled in yellow.

As one can see for the gamma events, the error values are quite small in the zones near one of the telescope and also in zones that are equidistant from at least two telescopes. But, if the core position is slightly closer to one telescope than the other ones, the errors are comparable to the distance to the closest detector. This might indicate that there exists some bias for that telescope, that "pulls" the core position to it.

On the other hand, for proton events, the values of the errors appear to be somewhat constant in the studied regions.

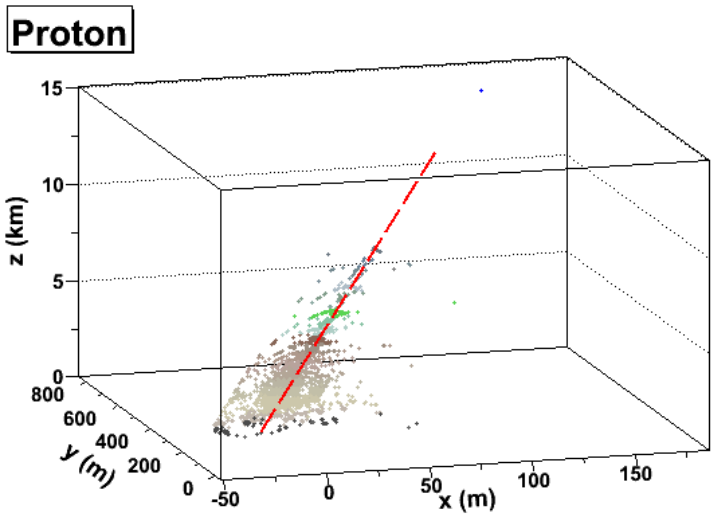

Figure 6.9: 3D reconstruction of a proton event

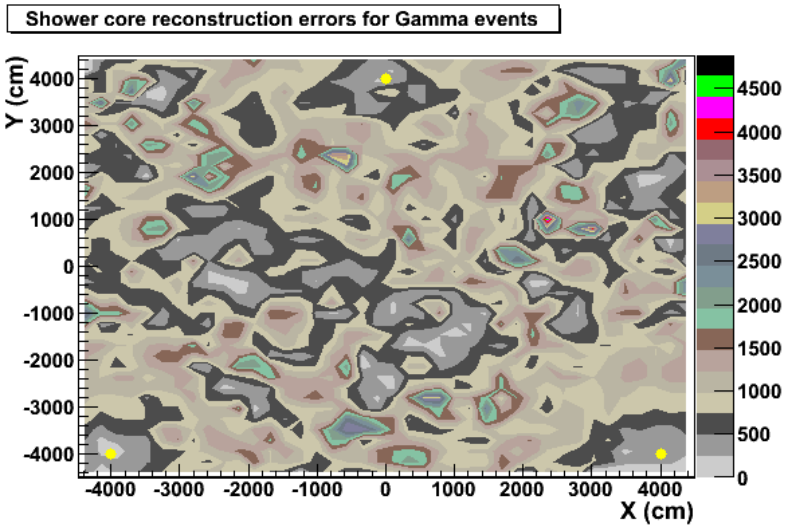

Figure 6.10: Core position errors as a function of real core position location for gamma events

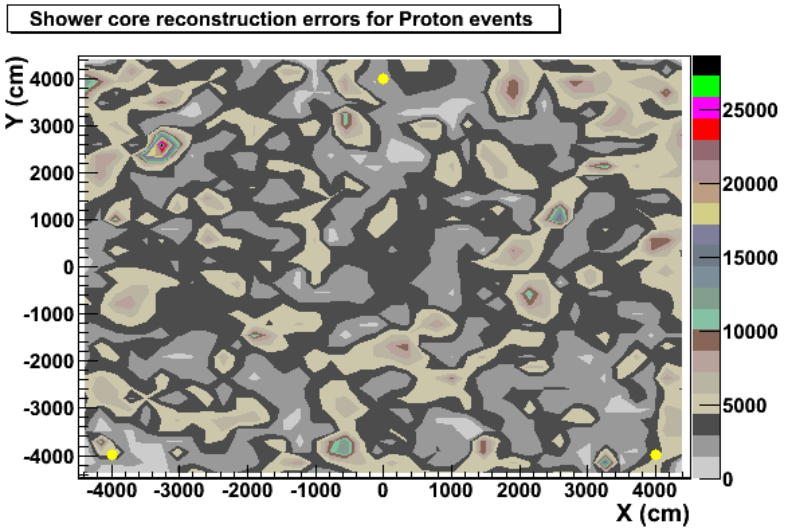

Figure 6.11: Core position errors as a function of real core position location for proton events

Chapter 7

Gamma/Proton Separation

The main purpose of Cherenkov Telescopes is the identification and study of Gamma-ray sources and, as such, pinpointing the direction of arrival of Gamma-ray particles using the collected Cherenkov Photons is crucial.

Since Proton and Gamma-ray Showers produce particles that, at high velocities, can emit Cherenkov light, the IACT telescopes will collect both types of showers. This becomes a problem if we have in mind that most of the collected showers will be of Proton type and so, correctly identifying the Gamma-ray Showers becomes mandatory.

These Proton Showers seemingly blend with the Electromagnetic Showers and can come from any direction. So far, techniques have been developed to distinguish one type of shower from the other but the creation of new methods and study variables might improve considerably the gamma/proton discrimination ratio.

In simple terms, the problem is that we have a few telescopes, each with a number of collected Cherenkov photons with known arrival direction and we have to retrieve two pieces of information:

- Where did the shower came from;
- Is it a Gamma-ray shower?

7.1 Classical Method

Various methods have been applied to answer these questions, using statistical pattern recognition, cluster analysis, computational geometry and others. The general framework of the method proposed for the GAW collaboration is [26]:

- Extraction of the useful information from each telescope;
- Determination of the major axis of each image, which should be the projection of the shower axis;
- Reconstruction of the air shower arrival direction;
- Reconstruction of the core location;
- Evaluation of the Hillas shape parameters from each image;
- Gamma-ray / Proton shower separation;

7.1.1 Extraction of the useful information from each telescope

The extraction of the useful information from each telescope consists of selecting the relevant pixels from the shower image using a single-link cluster analysis [25]. For each image we determine a Minimum

Spanning Tree (MST), which is a random graph that minimizes the sum of the weights of its edges, where the edge weight is the Euclidean distance between two nodes (or pixels) of the graph. Given a suitable cut-threshold ξ, the MST is separated in a Minimum Spanning Forest (MSF), as shown in the example of Fig.7.1. Each MSF' component is considered significant if it contains more than a minimum number of nodes (or pixels), and the significance can be evaluated making use of statistical considerations. The set of significant components of the MSF then constitute the group of relevant pixels which can be used to determine the characteristics of the shower image in each single telescope.

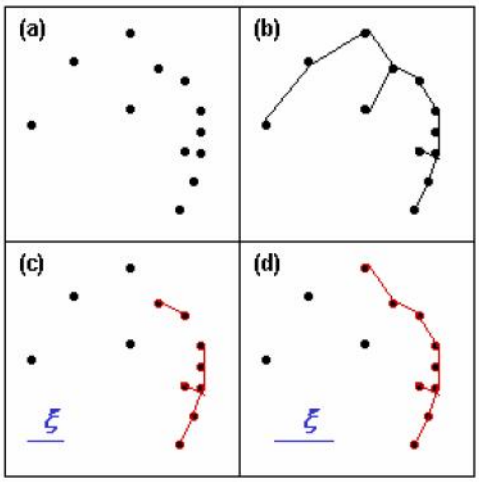

Figure 7.1: (a) Sample Data; (b) MST; (c,d) MSF at two different cut-threshold values [26]

These MST group together the relevant pixels for each telescope, which can then be used to determine the characteristics of the shower.

7.1.2 Determination of the major axis

Generally, the method applied for the determination of the major axis is based on the analytical solution of the Normalized Quadratic Axial Moments (NQAM), computed around the centroid of the image. This calculated using formula 7.1.

$$NQAM(j) = \frac{\mu_\alpha(j)}{Max\left\{\mu_\alpha(j), j = 1, NMOM\right\}} \tag{7.1}$$

Where μ_α is the second order momentum (given by 7.2) and X_c, Y_c are the coordinates of the centroid.

$$\mu_\alpha = \sum_{i=1}^{N} (\delta_{\mu_\alpha}(i))^2 \tag{7.2}$$

$$\delta_{\mu_\alpha}(i) = \frac{|(X_i - X_c)\tan(\alpha) - (Y_i - Y_c)|}{\sqrt{\tan^2(\alpha) + 1}} \tag{7.3}$$

The direction of the major axis is defined as the angle that minimizes the NAQM. The algorithm becomes simple and fast using the following definitions:

$$NQAM_{min} = \min\left\{NQAM(\alpha_1), NQAM(\alpha_2)\right\} \tag{7.4}$$

$$\alpha_{1,2} = \arctan\left(\frac{s_{y^2} - s_{x^2} \pm \Delta s}{2 s_{xy}}\right) \tag{7.5}$$

$$s_{x^2} = \sum_{i=1}^{N} (X_i - X_c)^2; \quad s_{y^2} = \sum_{i=1}^{N} (Y_i - Y_c)^2; \quad s_{xy} = \sum_{i=1}^{N} (X_i - X_c)(Y_i - Y_c); \tag{7.6}$$

$$\Delta s = \sqrt{(s_{x^2} - s_{y^2})^2 + 4{s_{xy}}^2} \tag{7.7}$$

7.1.3 Reconstruction of the shower direction

To reconstruct the air shower arrival direction we have to overlap the sky-view images of all the telescopes. The sky-view is the image that represents the directions of arrival of each pixel. In this view, we find the point that is closest to all of the major axis lines, which is the reconstructed shower direction. An example of these first steps is shown below (fig. 7.2).

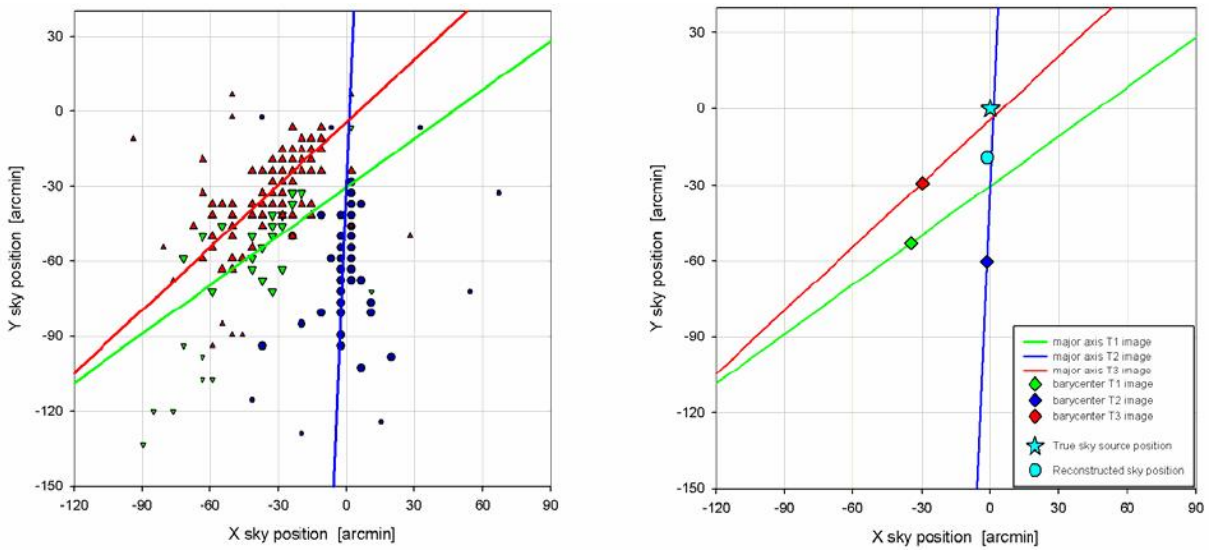

Figure 7.2: Reconstruction of the air shower arrival direction [26]

7.1.4 Reconstruction of the core position

The reconstruction of the core position follows the same principals used in the reconstruction of the shower direction. In this case we use the telescopes positions at ground level and the direction of the major axis of each telescope to define the lines that should point to the shower core.

The reconstructed shower core is then the point that is closest to all the lines.

7.1.5 The Hillas parameters

The Hillas parameters where first introduced in 1985 by M. Hillas in a paper in which he proposed that these images could be reduced to a set of numbers that described the two-dimensional ellipse figure visible in each image [27].

These parameters are the following (Fig. 7.3):

- $length$ is the Root Mean Square (RMS) spread of light in direction parallel to the major axis (RMS in respect with the minor axis);

- $width$ is the RMS spread of light in the direction perpendicular to the major axis (RMS in respect to the major axis);

- $distance$ is the angular displacement of the image centroid from the centre of the Field of View (FOV);

- $azimuthal\ width$ is the RMS image width with respect to the Distance axis;

- $miss$ is the perpendicular distance from the major axis to the centre of the FOV;

- $alpha$ is the angle between the major axis and the Distance axis.

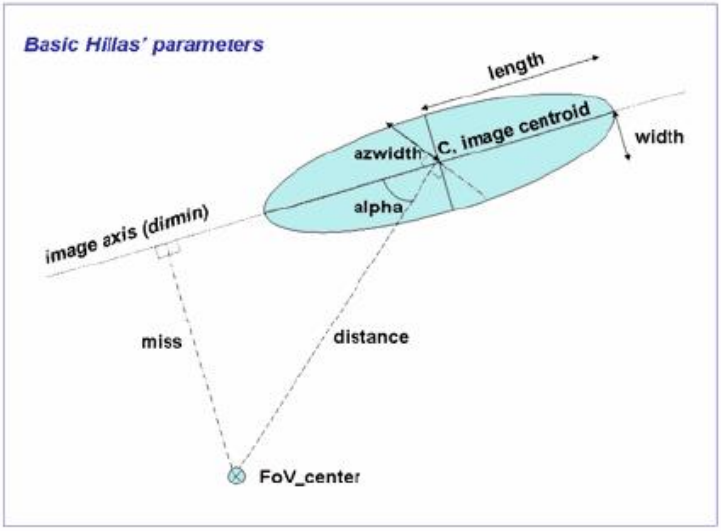

Figure 7.3: Description of the Hillas parameters [26]

7.1.6 Gamma-ray / Proton shower separation

Each of the telescopes used provides its own set of Hillas parameters. The variable that best describes the differences in γ-ray and proton showers is the $azimuthal\ width$, and a combination of all the telescopes can be achieved by means of a simple average.

A simulation of this separation method was performed for the GAW case. Results indicate that by performing a cut on $azimuthal\ width$ that ensures the mantenance of 60$\%$ of the simulated γ-rays, only 2.5$\%$ of protons showers survive the cut.

7.2 3D Separation Method

A new separation method that uses the α and b variables explained in chapter 5 is proposed. With the reconstructed shower direction and shower core, the distributions of these variables can be built for each telescope. Also, a radius R_i can be associated to each telescope, defined as the distance from the telescope to the core position.

Two different estimators were developed, using the second set of simulated showers, a χ^2 estimator and a likelihood one. The information needed for both is the same. First, the α and b cumulative functions are fitted with proper equations, and information is retrieved from each. For α, a variable that represents the location of the peak of Cherenkov emission is used, while for b the slope of the curve is used. These values are then divided by R dependant functions that represent the behaviour of the variable in the case of a γ or proton primary. The normalized values are then compared to normal distributions.

Both estimators can then be calculated, with each variable having an associated weight. These weights represent the capability of each variable to separate γ and proton showers at a fixed R.

A more detailed description follows.

7.2.1 Cumulative curves

An easy and coherent way to study both distributions is to build the cumulative curves for each telescope. Due to differences in the distributions of α and b, a different approach has to be taken for each.

From the α curves shown in chapter 5, one can see that the peaks are not symmetric. This can be understood, using fig. 3.4, as for each radius at ground level there are two different emission heights and, therefore, two different emission angles. Each of these angles will be associated to a peak. It is also known that the number of Cherenkov emitted for the smallest angle is higher due to the number of charged particles that exist at that height. The combination of both in the final spectrum hides the second peak in the tail of the first one, originating a big slope for small angles and a lower one for higher angles.

This can be measured in the cumulative curves using the fit function in eq. 7.8. The parameters τ_1 and τ_2 are measurements of the two slopes. While ω and ψ should resemble closely the location of the peaks. A can be understood as the intensity of one of the peaks, with $1 - A$ the intensity of the other one. Generally, and due to the initial conditions chosen for the fit, A will be the intensity of the lowest peak. Figure 7.4 shows the shape of the cumulative curves (black) and the fit performed with equation 7.8 (red), of one of the telescopes for a γ and a proton shower.

$$C_\alpha(\alpha) = 1 - \frac{1-A}{1+\exp(\frac{\alpha-\omega}{\tau_1})} - \frac{A}{1+\exp(\frac{\alpha-\psi}{\tau_2})} \tag{7.8}$$

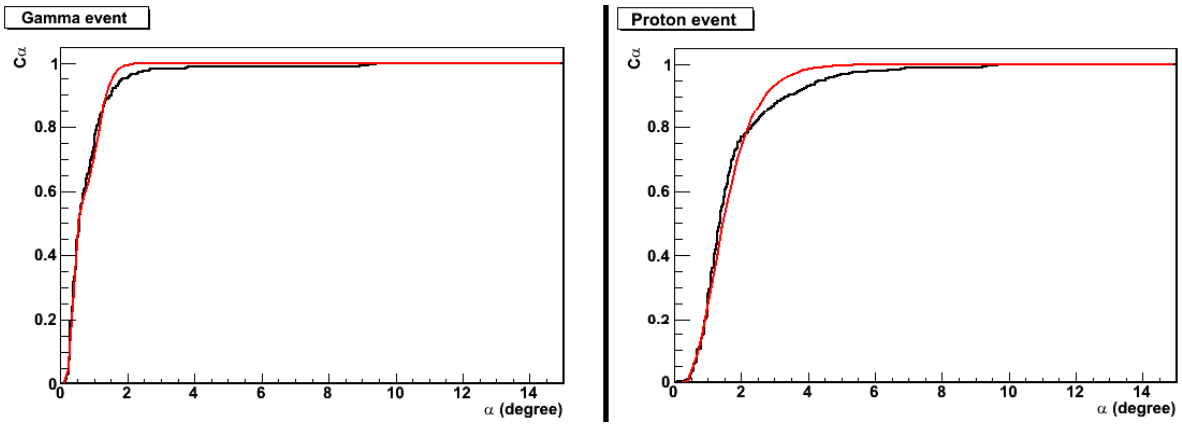

Figure 7.4: Fit of function C_α of a telescope for γ and proton showers

For b, the spectras are exponential decays with a pile-up at $b = R$ that should correspond to the integral of the exponential function from there to infinity. The cumulative distribution can then be fitted by eq. 7.9, where Δ is the decay rate. Figure 7.5 shows the cumulative curves (black) and the fit performed with equation 7.9 (red), of one of the telescopes for a γ and a proton shower.

$$C_b(R) = 1 - \exp\left(-\frac{R}{\Delta}\right) \tag{7.9}$$

7.2.2 Separation parameters

The variable in C_α that seemed to be more well-behaved for γ events was ω, while the others did not have such a compact distribution. Thus, using a set of simulated γ-ray and proton showers, the variables

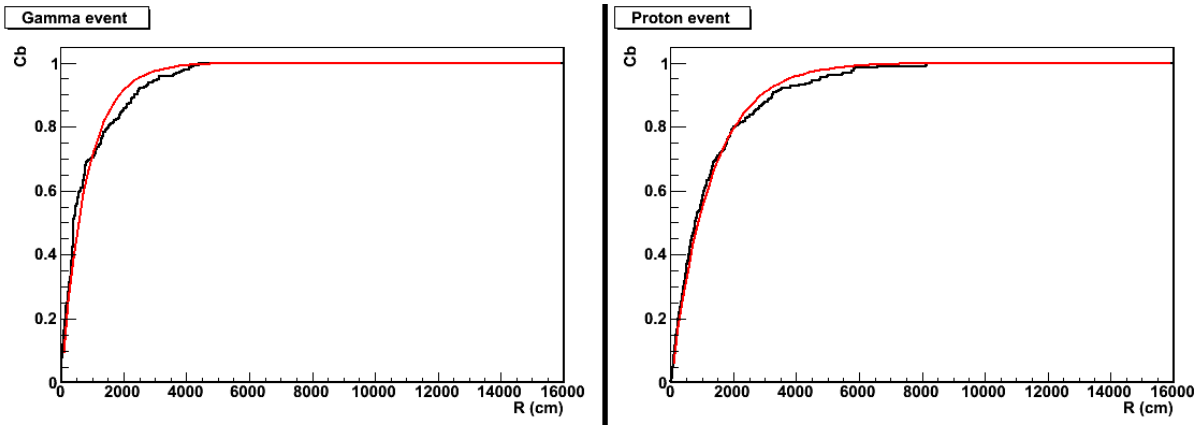

Figure 7.5: Fit of function C_b of a telescope for γ and proton showers

ω and Δ, respectively for the α and b distributions, were studied as a function of R. The results are shown in figures 7.6 and 7.7.

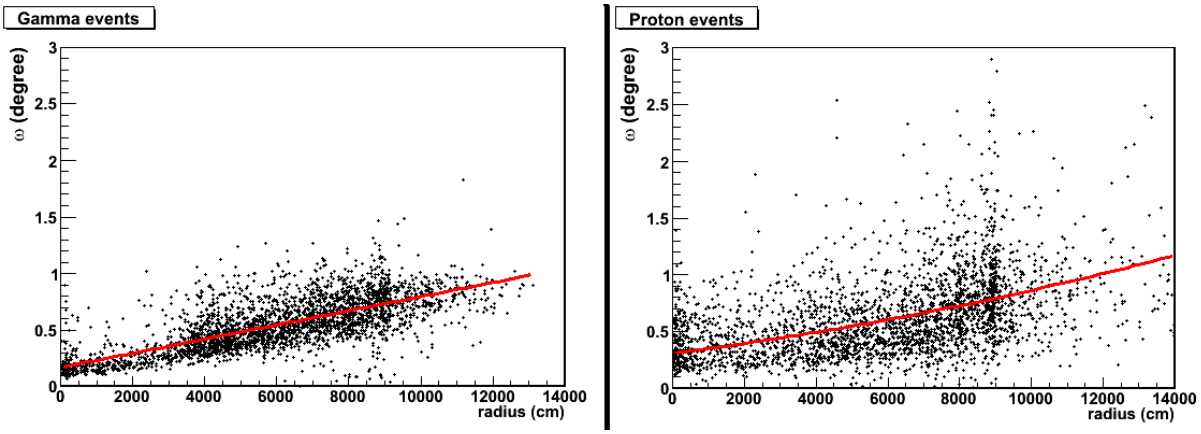

Figure 7.6: Distribution of ω for γ and proton showers

The functions obtained are the ones in equations 7.10 and 7.11, for α and b respectively, with the fit values shown in table 7.1.

$$F^{\omega}(R) = a_0 + \frac{R}{a_1} + \frac{R^2}{a_2} \tag{7.10}$$

$$F^{\Delta}(R) = b_0 \left(1 - \exp\left(-\frac{R}{b_1}\right)\right) \tag{7.11}$$

	a_0 (deg)	a_1 (cm deg^{-1})	a_2 (cm^2 deg^{-1})	b_0 (cm)	b_1 (cm)
Gamma-Ray	0.17	16000	4×10^{16}	1000	1000
Proton	0.31	25000	6.5×10^{8}	3000	2000

Table 7.1: Fit results

7.2.3 Approximation to Normals

With $F^{\omega}(R)$ and $F^{\Delta}(R)$, we have the expected values for both variables as a function of R. We can define ω^*_γ as $\omega/F^{\omega}_{\gamma}(R)$, ω^*_p as $\omega/F^{\omega}_{p}(R)$, Δ^*_γ as $\Delta/F^{\Delta}_{\gamma}(R)$ and Δ^*_p as $\Delta/F^{\Delta}_{p}(R)$. Figure 7.8 shows ω^*_γ

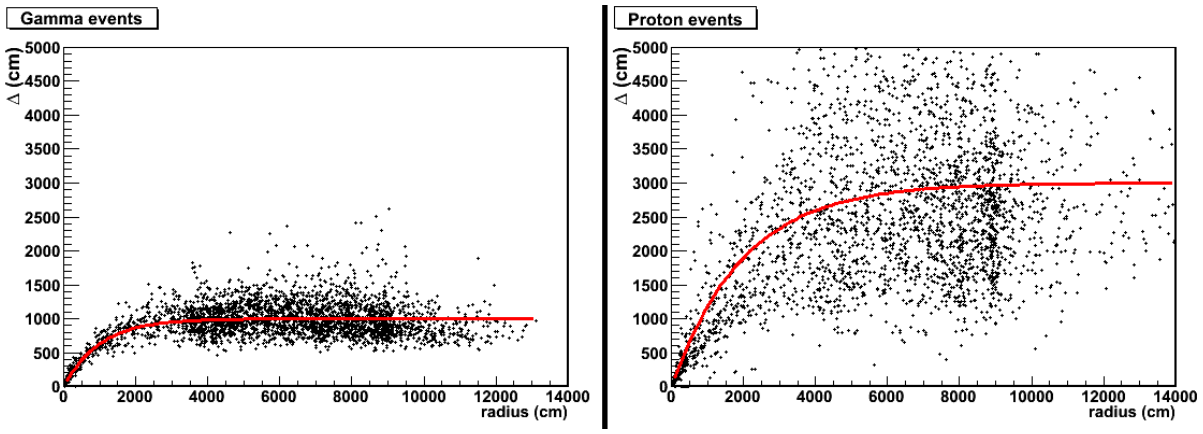

Figure 7.7: Distribution of Δ for γ and proton showers

for γ events and ω_p^* for proton showers, while figure 7.9 shows Δ_γ^* and Δ_p^* for γ and proton showers, respectively.

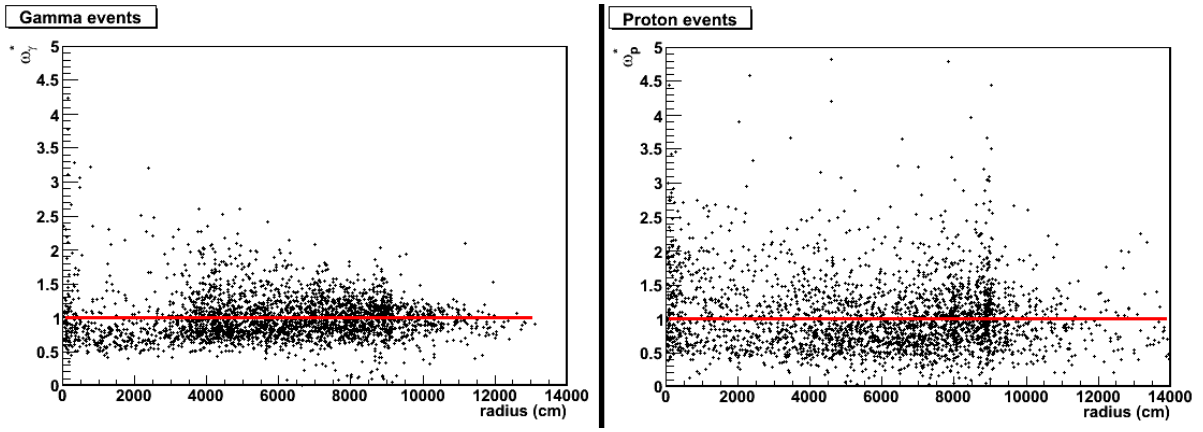

Figure 7.8: Distribution of ω_γ^* for γ showers and ω_p^* for proton showers

The distributions of these parameters are approximately Gaussian curves with an average value of 1. Figures 7.10 and 7.11 show the distributions as well as the fits performed. The standard deviation σ of each distribution can be found in table 7.2.

	σ^ω	σ^Δ
Gamma-Ray	0.25	0.25
Proton	0.4	0.4

Table 7.2: Sigma values

The values obtained for σ exemplify one of the main differences between γ and proton showers. While the distributions for γ events are compact and have small σ, the proton cases are more disperse having higher deviations.

7.2.4 Weights

For a given R, the sensitivity a variable has to separate γ from proton showers can be measured by comparing the γ curves with the proton ones. This comparison can be done by normalising the popula-

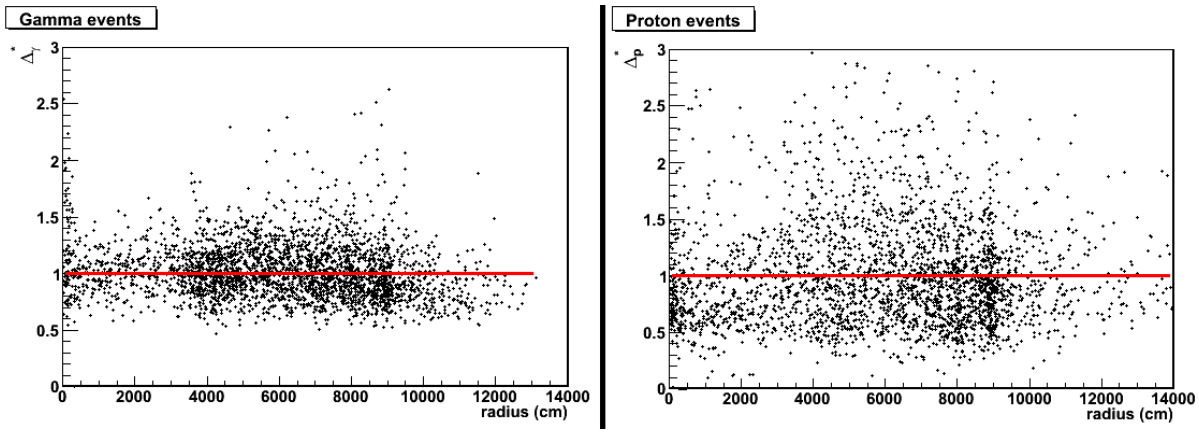

Figure 7.9: Distribution of Δ^*_γ for γ showers and Δ^*_p for proton showers

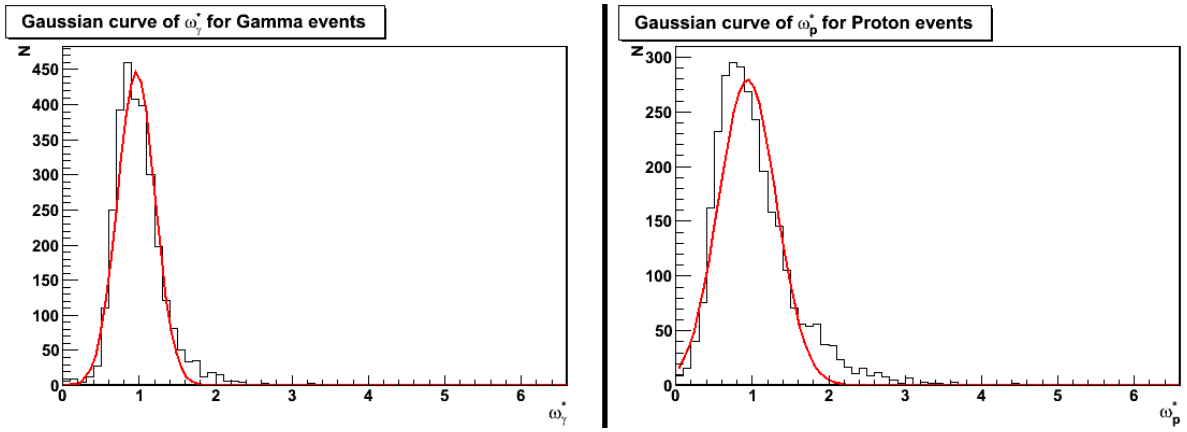

Figure 7.10: Distribution of ω^*_γ for γ showers and Δ^*_p for proton showers

tions of both variables (ω and Δ) to the expected values in the γ case ($F^\omega_\gamma(R)$ and $F^\Delta_\gamma(R)$). Figures 7.8 and 7.9 show the normalizations for the γ population (ω^*_γ and Δ^*_γ), while figure 7.12 shows the proton case for both variables.

The spread of the points has to be taken in consideration as well. For the γ cases this has already been calculated as σ^ω_γ and σ^Δ_γ. On the other hand, for the proton cases, the values of $\sigma^\omega_{p/\gamma}$ and $\sigma^\Delta_{p/\gamma}$ for slices of 10 m were calculated. Since these values were not constant with R, the functions that were found that best fitted those values are shown in equation 7.12.

$$\begin{aligned} \sigma^\omega_{p/\gamma}(R) &= 0.38 + \frac{330}{R+500} \\ \sigma^\Delta_{p/\gamma}(R) &= 0.334 + \left(\frac{R}{1950}\right)^{1.63} \times \exp\left(-\frac{R}{3250}\right) \end{aligned} \tag{7.12}$$

Using these values, we can introduce the relative importances W^ω and W^Δ that measure the discrimination power of each variable as a function of R. These functions will be used to weight the values of ω and Δ obtained, so to give more significance to the variable that best discriminates γ from protons at a specific R. These weights can be calculated using equations 7.13 and 7.14.

$$W^\omega(R) = \frac{\left|1 - \frac{F^\omega_p(R)}{F^\omega_\gamma(R)}\right|}{\sqrt{\left(\sigma^\omega_\gamma\right)^2 + \left(\sigma^\omega_{p/\gamma}(R)\right)^2}} \tag{7.13}$$

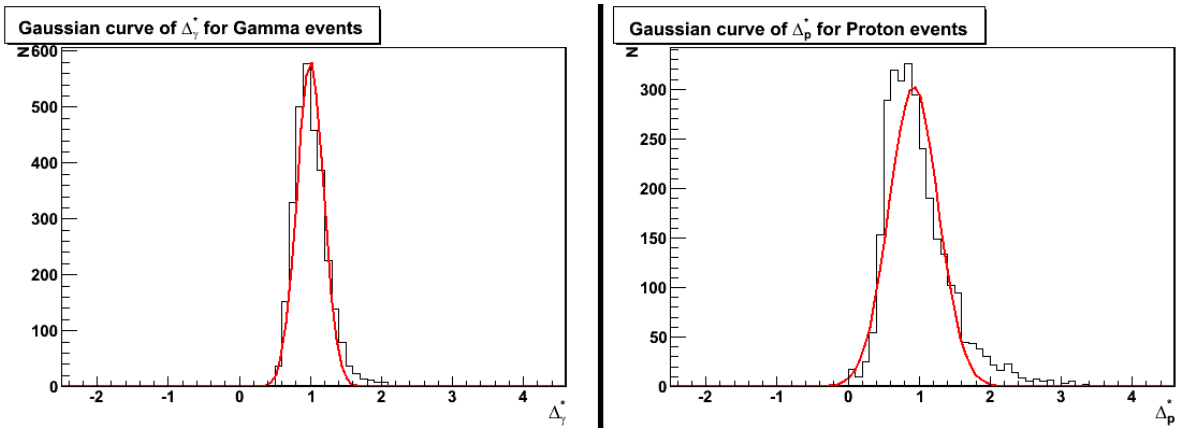

Figure 7.11: Distribution of Δ_γ^* for γ showers and Δ_p^* for proton showers

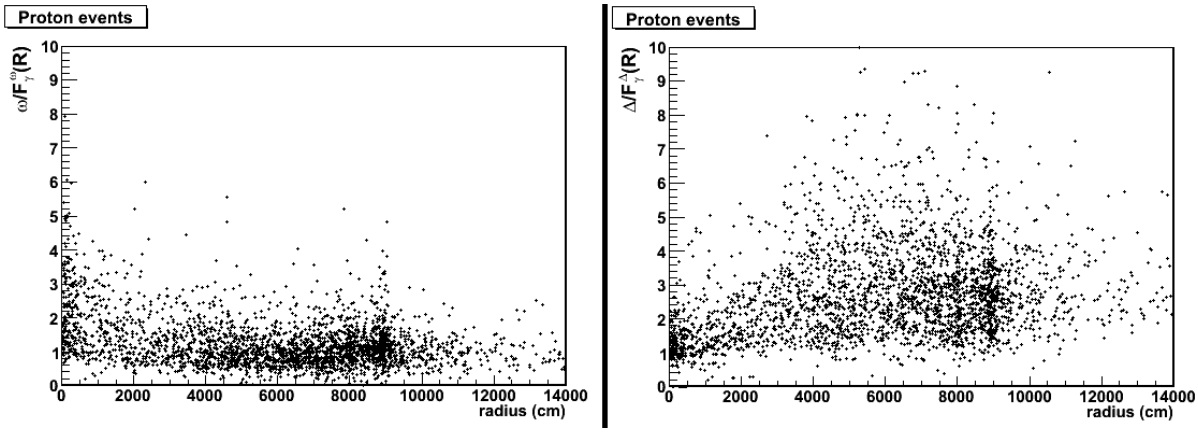

Figure 7.12: Normalization of ω with $F_\gamma^\omega(R)$ and of Δ with $F_\gamma^\Delta(R)$ for the proton cases

$$W^\Delta(R) = \frac{\left|1 - \frac{F_p^\Delta(R)}{F_\gamma^\Delta(R)}\right|}{\sqrt{\left(\sigma_\gamma^\Delta\right)^2 + \left(\sigma_{p/\gamma}^\Delta(R)\right)^2}} \tag{7.14}$$

Figure 7.13 shows the value of the weights as a function of R. While for ω the weight is small for every R, for Δ the weight increases with R. For small radius, both weights are comparable and as such both variables will be important. However, for medium and high R, the weight of Δ clearly surpasses that of ω, and so the impact parameter distribution will be much more relevant than the one for the angle of emission α.

7.2.5 χ^2 algorithm

The first proposed method to separate γ and proton showers is a χ^2 algorithm. This algorithm test the hypothesis of the shower being a γ shower, where χ^2 is a measure of how far from being a γ shower the event is. With N telescopes, the χ^2 can be calculated using equation 7.15.

$$\chi^2 = \frac{1}{\sum_{j=1}^{N}\left(W^\omega{}_j + W^\Delta{}_j\right)} \sum_{i=1}^{N}\left(W^\omega{}_i \times \left(\frac{\omega_{\gamma i}^* - 1}{\sigma_\gamma^\omega}\right)^2 + W^\Delta{}_i \times \left(\frac{\Delta_{\gamma i}^* - 1}{\sigma_\gamma^\Delta}\right)^2\right) \tag{7.15}$$

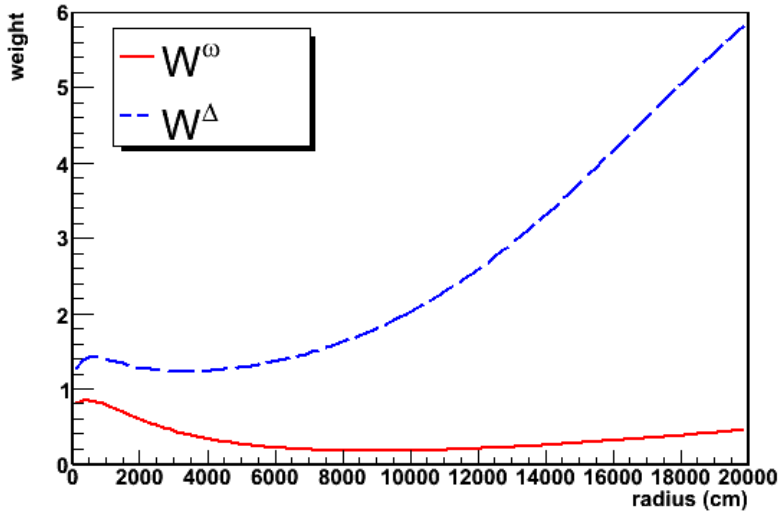

Figure 7.13: Weights of ω and Δ as a function of R

7.2.6 Likelihood algorithm

Admitting that the distributions of ω^* and Δ^*, for γ and proton cases, are Gaussian curves with average 1, the probability of belonging to a specific group can be calculated as twice the integral from that point to infinity. In case the point is below 1, a simple transformation $(2-x)$ finds the correspondent point that is higher than 1 and has the same value.

In practice, the probability can be calculated with equation 7.16. To normalize this integral, the result is divided by its expected value, given by equation 7.17.

$$P^{\omega^*,\Delta^*} = 1 - 2 \times \int_1^x \frac{1}{\sigma\sqrt{2\pi}} e^{-\frac{(x'-1)^2}{2\sigma^2}} dx' \tag{7.16}$$

$$E\left[P\right] = 2 \times \int_1^\infty \frac{1}{\sigma\sqrt{2\pi}} e^{-\frac{(x-1)^2}{2\sigma^2}} \left(1 - 2 \times \int_1^x \frac{1}{\sigma\sqrt{2\pi}} e^{-\frac{(x'-1)^2}{2\sigma^2}} dx'\right) dx = 0.5 \tag{7.17}$$

The normalized values of the integral for both variables as a function of the radius can be seen in figures 7.14 and 7.15.

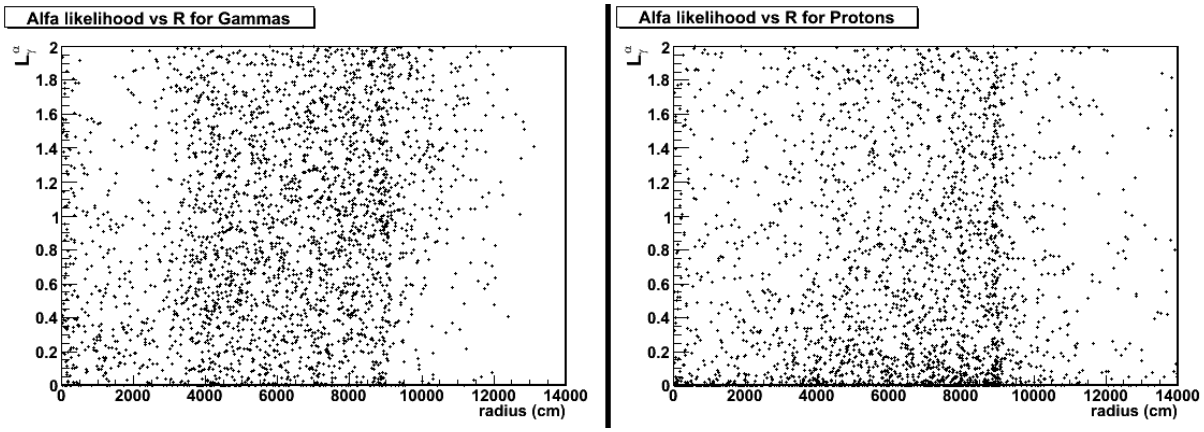

Figure 7.14: Gamma likelihood component of ω^* as a function of R for γ and proton showers

With the "probability" values, a likelihood function can be built as the product of those values. Analysing figures 7.14 and 7.15, it becomes clear that for R smaller than 2000 cm, roughly, Δ is not

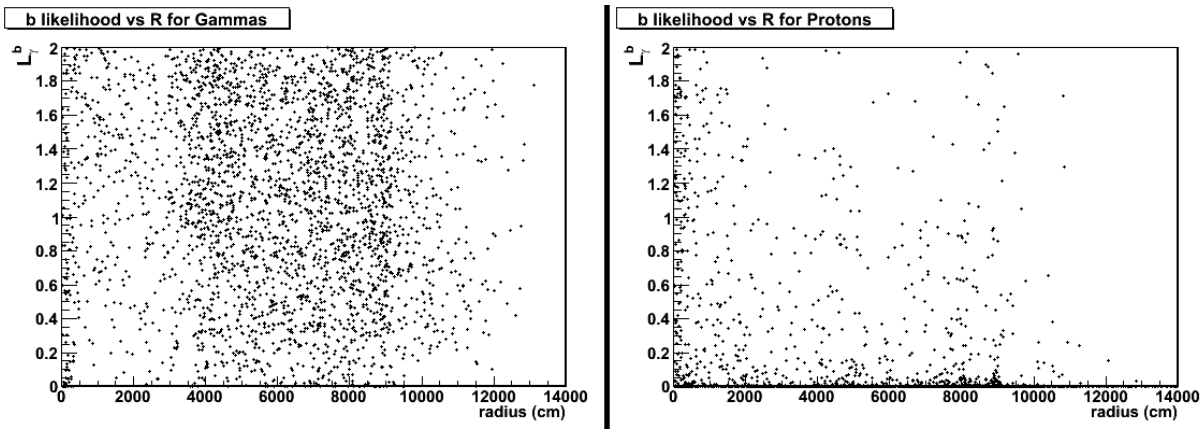

Figure 7.15: Gamma likelihood component of Δ^* as a function of R for γ and proton showers

as efficient at separating γ and protons as it is for higher values, since the integrals in the proton cases are not close to zero for a significant number of events. On the other hand, the capability that ω has of separating the two types of showers is clearly lower for high values of R. This comes in agreement with the weights given before, where for low radius both variables have approximately the same weight, while for medium and high R Δ is much more relevant.

For each event, the likelihood of being a γ-ray (L_γ) or proton (L_p) induced shower is calculated using equation 7.18, where N is the number of telescopes.

$$L_X = \frac{1}{E\left[P\right]}\left(\prod_{i=1}^{N}(P^{\omega^*_{X\,i}})^{W^{\omega}{}_i} \times (P^{\Delta^*_{X\,i}})^{W^{\Delta}{}_i}\right)^{\frac{1}{\sum_{j=1}^{N} W^{\omega}{}_j + W^{\Delta}{}_j}} \tag{7.18}$$

7.3 Results

With the third set of simulated showers, both estimators were studied. For each, a cut was defined that recognized around 80% of the γ showers as originated from γ-rays. The number of proton showers accepted with this cut was also studied.

7.3.1 χ^2 algorithm

The cumulative curves of the χ^2 values for γ and proton showers are shown in figure 7.16.

It is easily seen that most of the γ events have small values of χ^2, with 80% of them having values up to 1.5. Comparing with the proton showers, these have typically higher values. With values bellow 1.5, there are only 1% of proton events.

7.3.2 Likelihood algorithm

Figure 7.17 shows the values of L_γ and L_p obtained for γ and protons.

For the γ events, three important regions can be identified. The first, is defined by L_γ over 0.4 and L_p bellow 0.4, where most of the γ events are. The second and the third have L_γ smaller than 0.4 but while the second has L_p bellow 0.3, the third has L_p values over 0.3.

The first region is the "good" region for γ events, and an event that enters this region will be accepted as a γ shower. For this sample, 81.2% of the events are in this region.

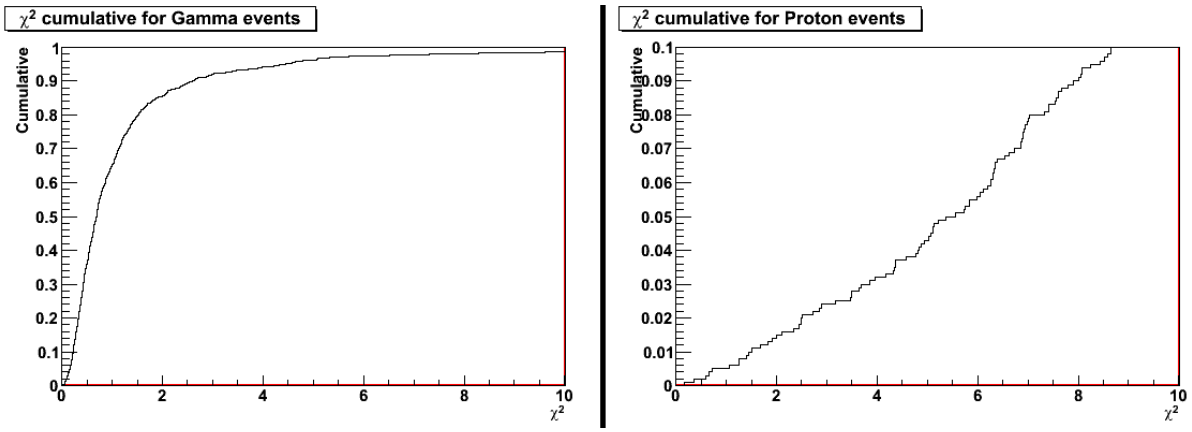

Figure 7.16: Cumulative curves of χ^2 for γ and proton showers

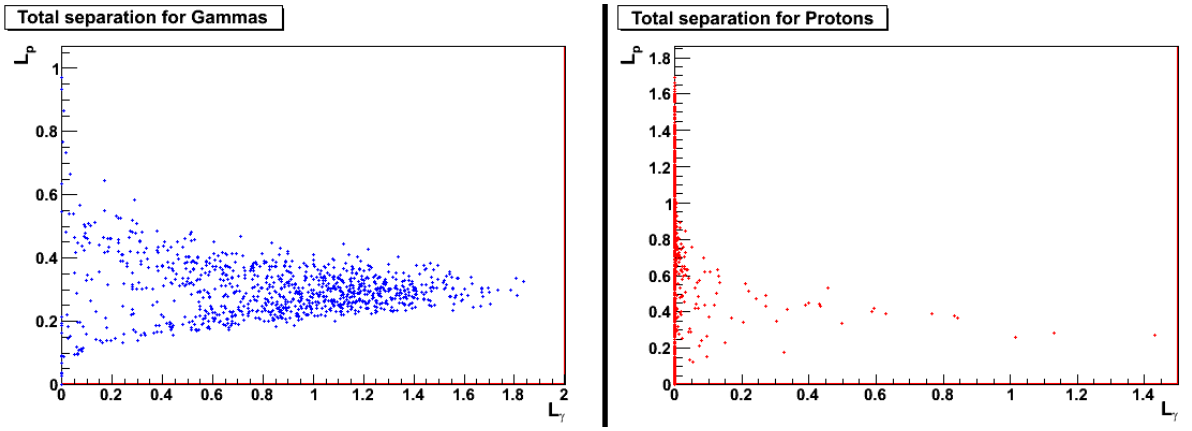

Figure 7.17: L_γ and L_p for γ and proton showers

The second region is characterized by an increase in L_p with the increase in L_γ, while in the third region L_p decreases with L_γ. As it has been seen, due to the weights introduced, Δ is the variable that most influence has on this calculation. Comparing the curves for γ and protons events of this variable, one can see that the proton curve is above the γ one. As such, when the points distance themselves from the average for lower values, L_γ decreases as does L_p. These are the points that belong to the second region. On the other hand, if they have higher values of Δ, L_γ decreases but L_p increases and thus they are situated in the third region.

The proton events are clearly distinguished by having very small values of L_γ. The few that have higher values are those that go well bellow the proton curve of F^Δ. The number of proton showers that belong to the first region, and hence the number of protons that are mistakenly taken as γ events, is very small. From the 1000 simulated showers only 8 are in this situation, corresponding to 0.8%.

Chapter 8

Conclusion

The main challenge in the detection of Very High Energy γ-ray sources, with IACTs, is the separation of γ events from proton showers. Solving this problem would allow a much more efficient source detection. Usually the Hillas parameters are used to identify the primary particle of a shower. Although being a good method, clearly it can be improved. An innovative 3D method was proposed in this work.

Two new 3D variables that characterize a shower seen by one telescope were introduced. The first is the distribution of the emission angles (α) of the Cherenkov photons in respect to the shower main axis. The second is the distribution of the impact parameters (b) of each arriving Cherenkov photon. b can be understood as an approximation to the distance between the emission point of the photon and the shower main axis.

However, to be able to calculate these variables, the shower main axis and core position must be known. A geometrical reconstruction method was then developed. On a first phase, this method combines the information of different telescopes to find an initial guess for the shower main axis and core position. Then, an iterative procedure begins that tries to minimize the values of the impact parameter. The iteration stops when the shower core position has converged.

The separation algorithm is based on both variables. The differences between γ and proton showers in α and b come primarily from the fact that proton showers are wider than γ showers. To measure these differences, two estimators were established. One is a χ^2 value that measures the differences between the current event and an average γ shower. The other one consists on calculating the likelihoods of the event being either a γ or a proton shower.

Some tests were performed on the reconstruction method, with the results showing small errors concerning the shower main axis for both types of showers. As for the shower core position, errors for γ events were about 10 meters, while for proton showers the errors were around twice this value.

80$\%$ of the γ events had a χ^2 value bellow 1.5 while, for the same region, there were only 1$\%$ of the simulated proton showers. For the likelihood algorithm, the good region for γ showers was found to be defined by $L_\gamma \geq 0.4$ and $L_p \leq 0.4$. This region contained 81.2$\%$ of the γ sample used, while only 0.8$\%$ of the protons were not cut.

Both estimators have very promising results, with the discrimination ratio higher than the one expected for GAW using the Hillas parameters [28]. Further improvements can be made to the reconstruction method, which might improve the distributions of α and b and hence allow a better separation, and also to the separation algorithms where better measurements of the differences can be found.

This work is then expected to be the basis for future γ and proton separation algorithms, allowing a more efficient search for VHE γ-ray sources to occur.

Bibliography

[1] A. de Angelis, seminar at LIP, *Astroparticle physics with high-energy photons. I-The physics*, Lisbon, 2007.

[2] Weekes, T. C., *Very High Energy Gamma-Ray Astronomy*, Institute of Physics Publishing, 2003.

[3] M. F. Cawley and T. C. Weekes, *Experim. Astronomy*, 6:7, 1995.

[4] NASA's Web Site on EGRET, http://cossc.gsfc.nasa.gov/docs/cgro/egret/egret_doc.html.

[5] Cawley, M.F., et al., *A high resolution imaging detector for TeV gamma-ray astronomy*, Exper. Astron., 1, 173-190, 1990.

[6] F. A. Aharonian, W. Hofmann, A. K. Konopelko, H. J. Volk, *The potential of ground based arrays of imaging atmospheric Cherenkov telescopes. I. Determination of shower parameters*, Astroparticle Physics, 6, 343-368, 1997.

[7] G. Mohanty, S. Biller, D. A. Carter-Lewis, D. J. Fegan, A. M. Hillas, R. C. Lamb, T. C. Weekes, M. West, J. Zweerink, *Measurement of TeV gamma-ray spectra with the Cherenkov imaging technique*, Astroparticle Physics, 9, 15-43, 1998.

[8] ESA's Web Site on INTEGRAL, http://sci.esa.int/science-e/www/area/index.cfm?fareaid=21.

[9] HESS Web Site, http://www.mpi-hd.mpg.de/hfm/HESS/HESS.html.

[10] MAGIC Web Site, http://wwwmagic.mppmu.mpg.de/index.en.html.

[11] VERITAS Web Site, http://veritas.sao.arizona.edu/component/option,com_frontpage/Itemid,1/.

[12] CANGAROO Web Site, http://icrhp9.icrr.u-tokyo.ac.jp/index.html.

[13] NASA's Web Site on GLAST, http://glast.gsfc.nasa.gov/.

[14] R. Cornils, K. Bernlohr, G. Heinzelmann, W. Hofmann, M. Panter for the H.E.S.S. Collaboration, *The optical system of the H.E.S.S. II telescope*, 29th International Cosmic Ray Conference, Pune, India, 2005.

[15] P. Vicent for the H.E.S.S. Collaboration, *H.E.S.S. Phase II*, 29th International Cosmic Ray Conference, Pune, India, 2005.

[16] CTA Web Site, http://www.mpi-hd.mpg.de/hfm/CTA/.

[17] MILAGRO Web Site, http://www.lanl.gov/milagro/index.shtml.

[18] S. Swordy, *The energy spectra and anisotropies of cosmic rays*, Space Science Reviews 99, pp85-94, 2001.

[19] NASA's Air Cherenkov Detectors Web Site, http://imagine.gsfc.nasa.gov/docs/science/how_l2/cerenkov.html.

[20] D. Heck, J. Knapp, *Extensive Air Shower Simulation with CORSIKA - A User's Guide*

[21] GAW Collaboration, *GAW - A very large field of view Imaging Atmospheric Cherenkov Telescope: Concept Design and Science Case*, 2005.

[22] Wikipedia Web Site on Blazars, http://en.wikipedia.org/wiki/Blazar.

[23] M. C. Maccarone, GAW Internal Report GAW-Rep-MCM-4/06, *Study of GAW Expected Performance. Part 1: Analysis at Trigger Level.*, 2006.

[24] GAW Collaboration, The GAW Official Web Site, http://gaw.iasf-palermo.inaf.it/, 2005.

[25] V. Di Gesu', M.C. Maccarone, *Features Selection and Possibility Theory*, Pattern Recognition, Vol.19, No.1, pp.63-72, 1986.

[26] M. C. Maccarone, GAW Internal Report GAW-Rep-MCM-0/06, *Exploratory Analysis Techniques and Serendipity Search in Small Data Sets. Application on GAW Simulation.*,2006.

[27] A. M. Hillas, *Space Science Rev.*, 75:17-30, 1996.

[28] M. C. Maccarone, P. Assis, O. Catalano, G. Cusumano, P. Gonçalves, M. Moles, M. Pimenta, A. Pina, B. Sacco, B. Tomé, *Expected performance of the GAW Cherenkov Telescopes Array. Simulation and Analysis*, 30th International Cosmic Ray Conference, Mérida, México, 2007.